

1 **A Remote Sensing Algorithm for the Quantifying Vertically-Resolved Cloud**
2 **Condensation Nuclei Number Concentrations from Spaceborne Lidar**
3 **Measurements**

Style Definition: Heading 1: Justified, Space Before: 0 pt, After: 1.2 line, Line spacing: Multiple 1.1 li

Deleted: Resolving

Deleted: Profile of

4 Piyushkumar N. Patel^{1,2,*}, Jonathan H. Jiang¹, Ritesh Gautam³, Harish Gadhavi⁴, Olga V.
5 Kalashnikova¹, Michael J. Garay¹, Lan Gao⁵, Feng Xu⁵, Ali H. Omar⁶

6
7 ¹Jet Propulsion Laboratory, California Institute of Technology, Pasadena, CA, USA

8 ²Oak Ridge Associated Universities, Oak Ridge, TN, USA

9 ³Environmental Defense Fund, Washington, DC, USA

10 ⁴Physical Research Laboratory, Ahmedabad, India

11 ⁵School of Meteorology, University of Oklahoma, OK, USA

12 ⁶Science Directorate, NASA Langley Research Center, Hampton, VA, USA

13

14 ***Corresponding Author:** Piyushkumar N. Patel, (piyushether@gmail.com,
15 piyushkumar.n.patel@jpl.nasa.gov)

16 **Keywords:** CCN, aerosol, cloud, CALIPSO, satellite, Lidar

17

18 **Abstract.** Cloud condensation nuclei (CCN) are mediators of aerosol-cloud interactions (ACI),
19 contributing to the largest uncertainties in the understandings of global climate change. We present
20 a novel remote sensing-based algorithm that quantifies the vertically-resolved CCN number
21 concentrations (N_{CCN}) using aerosol optical properties measured by a multiwavelength lidar. The
22 algorithm considers five distinct aerosol subtypes with bimodal size distributions. The inversion
23 used the look-up tables developed in this study, based on the observations from the Aerosol
24 Robotic Network to efficiently retrieve optimal particle size distributions from lidar
25 measurements. The method derives dry aerosol optical properties by implementing hygroscopic
26 enhancement factors to lidar measurements. The retrieved optically equivalent particle size
27 distributions and aerosol type dependent particle composition are utilized to calculate critical
28 diameter using the κ -Köhler theory and N_{CCN} at six supersaturations ranging from 0.07% to 1.0%.
29 Sensitivity analyses indicate that uncertainties in extinction coefficients and relative humidity
30 greatly influence the retrieval error in N_{CCN} . The potential of this algorithm is further evaluated by
31 retrieving N_{CCN} using airborne lidar from the NASA ORACLES campaign and validated against
32 simultaneous measurements from the CCN counter. The independent validation with robust
33 correlation demonstrates promising results. Furthermore, the N_{CCN} has been retrieved for the first
34 time using a proposed algorithm from spaceborne lidar - Cloud-Aerosol Lidar with Orthogonal
35 Polarization (CALIOP) - measurements. The application of this new capability demonstrates the
36 potential for constructing a 3D CCN climatology at a global scale, which help to better quantify
37 ACI effects and thus reduce the uncertainty in aerosol climate forcing.

40 **1 Introduction**

41 The Intergovernmental Panel on Climate Change (IPCC) report states that radiative forcing caused
42 by aerosol-cloud interactions (ACI), dominates the largest uncertainty, and remains the least well-
43 understood anthropogenic contribution to climate change (IPCC AR5, 2013). The uncertainty
44 mainly stems from the complicated processes of how aerosols impact the global cloud system.
45 Atmospheric aerosols allow for water vapor condensation under certain supersaturation (SS)
46 conditions and subsequently evolve into cloud droplets by serving as cloud condensation nuclei
47 (CCN). Anthropogenic emissions are a major source of CCN, facilitating the formation of cloud
48 droplets, thereby altering cloud properties, precipitation patterns, and hence the climate forcing
49 (Carslaw et al., 2010; Paasonen et al., 2013). Consequently, reducing the uncertainty associated
50 with ACI is crucial for increasing our confidence in predictions of global and regional climate
51 models (IPCC, 2014). The fundamental parameter for understanding the aerosol-cloud interaction
52 is the CCN concentrations (Rosenfeld et al., 2014). Determining CCN number concentration
53 (N_{CCN}) is the basis for analyses of ACI (Seinfeld et al., 2016). Large uncertainties in their
54 magnitude and variability at a global scale are one of the main factors for the low level of scientific
55 understanding of ACI effects. Therefore, knowledge of the global abundance of aerosols capable
56 of serving as CCN is fundamental to advancing our understanding of ACI (Fan et al., 2016).

57 Tackling the challenges in climate change, as identified by the IPCC, requires that CCN properties
58 be measured globally. Missing such a fundamental quantity has greatly hindered our ability to
59 accurately quantify the effects of anthropogenic aerosols on cloud properties (Rosenfeld et al.,
60 2014). Ground-based instruments can observe N_{CCN} at various SS, but they only provide sparse
61 and localized information. Besides limited coverage, near-surface CCN properties could differ
62 significantly from CCN properties near the cloud base due to vertical aerosol inhomogeneities,
63 particularly under stable atmospheric boundary conditions. Airborne observations can provide
64 very useful CCN measurements near cloud base but are expensive to collect and are limited to a
65 few field experiments, and having limited spatial-temporal coverage (Feingold et al., 1998; Li,
66 Liu, et al., 2015; Li, Yin, et al., 2015).

67 Overall, observations of CCN are spatiotemporally sparse, lack the vertical dimension, and provide
68 insufficient constraints on their global distribution. ACI studies often use satellite retrievals to take
69 advantage of their global coverage, but satellites have been unable to measure the CCN.
70 Nevertheless, the aerosol optical parameters such as aerosol optical depth (AOD) and aerosol index
71 (AI) are commonly used as proxies for CCN in previous studies (Gryspeerd & Stier, 2012; Patel
72 et al., 2017, 2019; Patel & Kumar, 2016; Quaas et al., 2008, 2009; Rosenfeld, 2008). However, all
73 these proxies are crude tools and suffer from various issues such as aerosol swelling, lack of
74 vertical information, cloud contamination, uncertainty in size distribution and solubility, and more
75 (Rosenfeld et al., 2016). The aforementioned studies based on passive satellite remote sensing
76 measurements, such as AOD and AI have limitations in several areas for ACI studies.

77 Active remote sensing technologies such as lidar have the ability to improve the precision and
78 range of conditions under which particle concentrations and their ability to act as CCN can be
79 retrieved. A significant body of prior studies has assessed the relationship between aerosol optical

Deleted: (IPCC AR5, 2013)

Deleted: the

Deleted: (Carslaw et al., 2010; Paasonen et al., 2013)

Deleted: (IPCC, 2014)

Deleted: relevant for

Deleted: (Rosenfeld et al., 2014)

Deleted: (Seinfeld et al., 2016)

Deleted: (Fan et al., 2016)

Deleted: (Rosenfeld et al., 2014).

Deleted: (Feingold et al., 1998; Li, Liu, et al., 2015; Li, Yin, et al., 2015)

Deleted: (Gryspeerd & Stier, 2012; Patel et al., 2017, 2019; Patel & Kumar, 2016; Quaas et al., 2008, 2009; Rosenfeld, 2008)...

Deleted: (Rosenfeld et al., 2016)

95 properties and CCN based on local in situ data offered by lidar and radar. Feingold et al., (1998),
96 developed a technique to derive CCN from the retrieved cloud droplet concentration, vertical
97 velocity, and lidar backscatter from ground-based radar, lidar, and radiometer. Ghan et al., (2006)
98 and Ghan & Collins, (2004), evaluated the relationship between aerosol extinction from airborne
99 lidar and N_{CCN} from near-surface measurements and devised a technique for estimating CCN at a
100 cloud base. However, their techniques rely on the assumption that the physiochemical
101 characteristics of aerosols at the surface represent the vertical column. Thus, their retrievals may
102 be subject to large uncertainties due to vertical inhomogeneity in particle characteristics. Previous
103 work by Clarke & Kapustin, (2010); Kapustin et al., (2006); Liu & Li, (2014); Shinozuka et al.,
104 (2015), demonstrated a strong correlation between extinction coefficients and N_{CCN} instead of
105 vertically integrated AOD or AI using airborne and in situ observations. Stier, (2016), provided a
106 global assessment of the link between aerosol radiative properties and CCN using a global aerosol-
107 climate model (ECHAM-HAM) and suggested that vertically integrated aerosol radiative
108 properties are of limited suitability as a proxy for global surface CCN.

109 Both Mamouri and Ansmann, (2016) and Choudhury and Tesche, (2022), examine the potential of
110 single wavelength lidar observations to retrieve CCN number concentrations for different aerosol
111 types. The relationships between particle extinction coefficients and number concentrations of
112 particles with a dry radius larger than 50 nm (for non-dust) and 100 nm (for dust) were
113 parameterized based on multiyear AERONET observations for different aerosol types. However,
114 the measurements from the single wavelength lidar also lack sufficient information to quantify
115 particle size distribution, particle number concentration or aerosol type, resulting in large
116 uncertainty in N_{CCN} retrieval (Burton et al., 2012; Tan et al., 2019). However, few recent studies
117 (Lv et al., 2018; Tan et al., 2019), have shown efforts to retrieve N_{CCN} based on the advanced
118 capability of multiwavelength lidar measurements, but they have been limited to ground-based
119 observations only. Rosenfeld et al., (2016), have attempted a new approach to retrieve satellite
120 based N_{CCN} using passive satellite observations. All these studies taken together provide a sound
121 foundation of CCN-relevant aerosol properties, but most of them do not refer to CCN
122 concentrations themselves, and the ones who do, do not give a global coverage nor a vertically
123 resolved picture. Consequently, no reliable global observational data set of CCN exists, and the
124 ability to routinely measure vertically resolved CCN to study ACI effectively is still lacking
125 (Burkart et al., 2011).

126 This study introduces ECLiAP (*Estimation of CCN using Lidar measured Aerosol optical*
127 *Properties*), a comprehensive remote sensing algorithm designed to estimate the concentration of
128 cloud condensation nuclei (N_{CCN}) using multiwavelength spaceborne lidar measurements.

129 This paper is structured as follows: The introductory section discusses the importance and
130 motivation behind NCCN estimation. Section 2 describes the LUT-based approach utilized for
131 NCCN estimation, focusing specifically on satellite observations. Section 3 encompasses
132 numerical simulations, sensitivity analysis, extensive validation efforts, and an observational case
133 study. Finally, Section 4 comprehensively discusses the results and their broader implications.

134

Deleted: Feingold et al., (1998)

Deleted: Ghan et al., (2006) and Ghan & Collins, (2004)

Deleted: Clarke & Kapustin, (2010); Kapustin et al., (2006);
Liu & Li, (2014); Shinozuka et al., (2015)

Deleted: Stier, (2016)

Deleted: Mamouri and Ansmann, (2016) and Choudhury
and Tesche, (2022)...

Deleted: (Burton et al., 2012; Tan et al., 2019)

Deleted: (Lv et al., 2018; Tan et al., 2019)

Deleted: Rosenfeld et al., (2016)

Deleted: (Burkart et al., 2011)

Formatted: Font: Bold, Italic

Formatted: Font: Italic

Formatted: Font: Bold, Italic

Formatted: Font: Italic

Formatted: Font: Bold, Italic

Formatted: Font: Italic

Formatted: Font: Bold, Italic

Formatted: Font: Italic

Formatted: Font: Bold, Italic

Formatted: Font: Italic

Formatted: Subscript

Deleted: In this study, we developed a comprehensive remote sensing algorithm with a novel retrieval approach, known as ECLiAP (*Estimation of CCN using Lidar measured Aerosol optical Properties*), to estimate N_{CCN} from multiwavelength spaceborne lidar measurements. The approach is implemented with look-up table (LUT) involving aerosol size and composition information, in order to provide stable and efficient vertically-resolved CCN retrievals. The N_{CCN} at six critical supersaturations ranging from 0.07%-1.0% is determined from the retrieved particle size distributions. The retrieval accuracy is assessed using simulated lidar backscatter and extinction coefficients with both random and systematic errors. The structure of this paper is as follows: This section provides the importance and motivation for retrieving N_{CCN} . Section 2 discusses the inversion approach for retrieving N_{CCN} (particularly from satellite observations). The numerical simulations for the sensitivity analysis, an extensive validation effort, and an observational case study is presented in section 3. Section 4 covers the final discussion.

Formatted: Font:

166 **2 Dataset**

167 **2.1 NASA Observations of Aerosols above Clouds and their Interactions (ORACLES)**

Formatted: Font: Font color: Text 1

168 The NASA Observations of Aerosols above Clouds and their Interactions (ORACLES)
169 campaign, conducted between 2016 and 2018 over the southeast Atlantic (SEA) (Redemann et al.,
170 2021), provided valuable insights into a crucial region characterized by the interaction of biomass
171 burning emissions with marine stratocumulus clouds specifically during July to October. These
172 clouds wield significant influence over global climate; however, climate models often
173 inadequately represent them due to their abundance and brightness (Bony & Dufresne, 2005; Nam
174 et al., 2012). Furthermore, the challenges of non-polarimetric passive remote sensing of aerosols
175 in the presence of low stratocumulus clouds (Chang et al., 2021; Coddington et al., 2010)
176 underscore the criticality of accurately predicting Cloud Condensation Nuclei (CCN)
177 concentrations and refining model parameterization for the SEA region. To address the knowledge
178 gaps, the ORACLES campaign focused on comprehensive observations of aerosol and cloud
179 properties, employing a combination of remote sensing and in situ instruments aboard the NASA
180 P-3 (operational from 2016 to 2018) and ER2 (operational in 2016) aircraft. The ORACLES data
181 includes in-situ measurements of N_{CCN} from the CCN counter, as well as lidar measurements
182 obtained through NASA Langley Research Center's high-spectral resolution lidar (HSRL-2). We
183 seized this opportunity to conduct a validation exercise based on the accessible data.
184

185 **2.1.1 High-Spectral Resolution Lidar (HSRL)-2**

Formatted: Heading 3

186 The NASA Langley Research Center HSRL-2 measures aerosol backscatter and depolarization at
187 three wavelengths (355 nm, 532 nm, and 1064 nm) and aerosol extinction at 355 nm and 532 nm
188 using the HSRL technique (Burton et al., 2018; Shipley et al., 1983). At 1064 nm, extinction is
189 derived from the product of aerosol backscatter at 1064nm and an inferred lidar ratio at 1064 nm.
190 The HSRL-2 measurement technique differentiates between aerosol and molecular returns by
191 analyzing the spectral distribution of the return signal. Consequently, this enables the independent
192 determination of aerosol backscatter and extinction coefficients, unlike traditional elastic
193 backscatter lidar retrievals that rely on a lidar ratio assumption (Hair et al., 2008). The addition of
194 the 355 nm channel in HSRL-2 enhances sensitivity to smaller particles, including CCN, which
195 are crucial in aerosol-cloud interactions (Burton et al., 2018). The instrument achieves horizontal
196 and vertical resolutions of approximately 2 km and 15 m, respectively, for aerosol backscatter and
197 depolarization. For aerosol extinction coefficients, horizontal and vertical resolutions are
198 approximately 12 km and 300 m, respectively, with interpolation to match the finer resolutions of
199 backscatter and depolarization. In terms of temporal resolution, aerosol backscatter and extinction
200 coefficients are available at approximately 10 s and 60 s intervals, respectively. The uncertainty in
201 lidar observables, influenced by factors like contrast ratio and aerosol loading, can be within 5%
202 under certain conditions (Burton et al., 2018). This manuscript delves the ability of ECLiAP by
203 leveraging the advanced capabilities of HSRL-2, in accurately deriving N_{CCN} in the real-world
204 atmospheric conditions.

205 2.1.2 CCN counter

206 We utilize the Georgia Institute of Technology (GIT) Droplet Measurement Technologies (DMT)
207 CCN counter (CCN-100) as another primary instrument and data source. The CCN-100 facilitates
208 in situ measurements of CCN concentration across a range of water vapor supersaturation levels
209 (S), specifically between 0.1% and 0.4% (Kacarab et al., 2020; Redemann et al., 2021). The CCN-
210 100 is ingeniously designed as a continuous-flow streamwise thermal-gradient chamber
211 (CFSTGC) following the framework proposed by Roberts & Nenes, (2005). In this configuration,
212 a cylindrical flow chamber generates quasi-uniform supersaturation at its centerline through
213 continuous heat and water vapor transport from the wetted walls, subject to a temperature gradient.
214 The difference in heat and water vapor diffusivity in the radial direction ensures the generation of
215 supersaturation at varying levels depending on the flow rate and temperature gradient. An
216 advantage of the continuous-flow system is its rapid sampling capabilities, achieving a frequency
217 of approximately 1 Hz (Roberts & Nenes, 2005). Such high frequency is crucial for effectively
218 capturing rapidly changing environments, typical of airborne sampling scenarios. Aerosols that
219 activate into droplets with a radius greater than 0.5 μm are counted as CCN at the end of the growth
220 chamber. The horizontal resolution of in situ observations during the ORACLES campaign is
221 contingent upon aircraft speed. For accuracy, the uncertainty associated with CCN number
222 concentration is approximately $\pm 10\%$ at high signal-to-noise ratio (S/N), while the supersaturation
223 uncertainty is around $\pm 0.04\%$ (Rose et al., 2008). These precision values assure the reliability of
224 the CCN measurements, ensuring the robustness of the dataset used to validate the ECLiAP
225 derived N_{CCN} in our investigation.

227 2.2 Cloud-Aerosol Lidar and Infrared Pathfinder Satellite Observations (CALIPSO)

228 The CALIOP (Cloud-Aerosol Lidar with Orthogonal Polarization) on the CALIPSO satellite, the
229 first spaceborne polarization lidar, was launched in April 2006 (Winker et al., 2007). CALIPSO is
230 in 705 km sun-synchronous polar orbit, and the orbit is controlled to repeat the same ground track
231 every 16 days with cross-track errors of less than ± 10 km. CALIOP acquires high-resolution
232 (vertical and horizontal at 30 and 333 m below 8.2 km, and 60 and 1000 m between 8.2 and 20.2
233 km) profiles of total attenuated backscatter by aerosols and clouds at 532 and 1064 nm during both
234 day and night. Spatial averaging over different scale is typically performed to improve the signal-
235 to-noise ratio for reliable retrievals. For our study, we used the CALIPSO version 4.20 level 2
236 aerosol profile product (vertical and horizontal resolution: 60 m \times 5 km, temporal resolution: 5.92
237 s). The CALIOP first classified the aerosol and cloud layers using Clod-Aerosol Discrimination
238 (CAD) score algorithm (Liu et al., 2009). Further, the aerosol layers categorize into the subsequent
239 aerosol types (Omar et al., 2009). The hybrid extinction retrieval algorithms is used to retrieve the
240 aerosol extinction, using the assumed lidar ratios appropriate for each aerosol type (Young &
241 Vaughan, 2009) reported in the CALIPSO level-2 5 km aerosol profile product (Vaughan et al.,
242 2017). The determination of lidar ratio contributes the major uncertainty in the retrieval of
243 CALIOP aerosol extinction, and the misclassification of aerosol type is another source of
244 uncertainty (Yu et al., 2010). We incorporate the profiles of aerosol extinction coefficient,

Formatted: Font:

Formatted: Heading 3

Formatted: Font color: Black

Formatted: Heading 2, Space After: 1.2 line, Line spacing: Multiple 1.1 li

Deleted: (Winker et al., 2007)

Formatted: Font color: Black

Formatted: Font color: Black

Formatted: Font:

Deleted: (Stuart A. Young & Vaughan, 2009)

Deleted: (M. Vaughan et al., 2017)

Deleted: (Yu et al., 2010)

249 backscatter coefficient, and particle depolarization ratio, along with aerosol subtype information
250 from CALIOP, into the ECLiAP for the N_{CCN} retrieval. Additionally, we utilize relative humidity
251 profiles obtained from the Global Modelling and Assimilation Office Data Assimilation System
252 (Molod et al., 2015), which are included in the CALIPSO data product. We employed CALIOP
253 data to assess the N_{CCN} retrieval capability of ECLiAP and also conducted a case study.

Formatted: Font color: Black

254

Formatted: Normal, Justified

255 3 Methodology

256 3.1 Construction of Lookup Tables

257 The inversion solution using the combination of simultaneous measurements of backscatters at
258 three wavelengths and extinction at two wavelengths, also called $3\beta+2\alpha$, using lidar has been
259 gaining prominence for aerosol microphysical (effective radius, total number, volume
260 concentration, refractive index) retrieval (Burton et al., 2016; Müller et al., 1999, 2005, 2016;
261 Veselovskii et al., 2002, 2004, 2012). Several fundamental aspects of the mathematical problem
262 must be solved during the retrieval from multiwavelength lidar. The most important aspect is that
263 the inversion solution is not unique. The non-uniqueness of an inversion solution in the advanced
264 $3\beta+2\alpha$ technique is the primary source of the retrieval challenges (Chemyakin et al., 2016).
265 Additionally, retrieving six size parameters (number concentrations, effective radius, and
266 geometric standard deviation for fine and coarse mode particles) for a bimodal particle size
267 distribution (PSD) from five known quantities (β_{355} , β_{532} , β_{1064} , α_{355} , α_{532}) is still an ill-posed
268 inversion problem. Besides, the existing spaceborne lidar instrument (CALIOP onboard
269 CALIPSO) provides the measurements at only two wavelengths (532 nm & 1064 nm). Considering
270 all these constraints and partially compensating for the non-uniqueness problem, we employed the
271 LUT approach with a fine step of bimodal particle size distributions (PSDs) to derive aerosol size
272 parameters. The parameterization of bimodal lognormal PSD is described in section 2.1.1. The
273 fundamental design of the LUTs framework for lidar measurements builds to test the aerosol
274 optical properties that we target for precise information.

Deleted: (Burton et al., 2016; Müller et al., 1999, 2005, 2016; Veselovskii et al., 2002, 2004, 2012)

Deleted: that has to

Deleted: (Chemyakin et al., 2016)

275 In the present study, the LUTs are designed using the $3\beta+3\alpha$ (β_{355} , β_{532} , β_{1064} , α_{355} , α_{532} , α_{1064})
276 technique for the individual aerosol types. An additional input at a longer wavelength improves
277 the retrieval accuracy for coarse mode particles (Lv et al., 2018). These LUTs contain aerosol
278 optical properties such as backscatter coefficients at 355, 532, and 1064 nm (β_{355} , β_{532} , β_{1064}) and
279 extinction coefficients at 355, 532, and 1064 nm (α_{355} , α_{532} , α_{1064}), along with size parameters
280 including number concentration, effective radius and geometric standard deviation for fine and
281 coarse mode particles (N_{if} , r_f , σ_f , N_{ic} , r_c , σ_c). Primarily, the LUTs are generated for the five distinct
282 aerosol subtypes: marine, dust, polluted continental, clean continental, and smoke aerosols (as
283 shown in Figure 1). This study considers dust particles to be spheroid, while other aerosol types to
284 be spheres. The particle optical properties are computed using the well-known Mie scattering
285 theory (Bohren & Huffman, 1998) for spherical particles, which is a numerically accurate approach
286 over a wide range of particle sizes. Meanwhile, the T-Matrix method (Mishchenko & Travis, 1998),

Deleted: (Lv et al., 2018)

Deleted: aerosols

Deleted: (Bohren & Huffman, 1998)

Deleted: (Mishchenko & Travis, 1998)

295 is adopted for the spheroids, which is numerically precise for the limited particle sizes.
 296 Consequently, the improved geometric optics method (IGOM; [Bi et al., 2009](#); [Yang et al., 2007](#)),
 297 is applied to the larger spheroids not covered by the T-matrix method. The axis ratio distribution
 298 for spheroids, ranging from ~0.3 (flattened spheroids) to ~3.0 (elongated spheroids) is taken from
 299 [Dubovik et al., \(2006\)](#). ~~The transition from the TMM to IGOM is determined by specific size~~
 300 ~~parameters and is dependent on the particle shape and refractive index. However, the present study~~
 301 ~~considers the mean complex refractive index, the transition from TMM to IGOM depends on the~~
 302 ~~particle shape.~~ PSD and mean complex refractive index were used as the input parameters for the
 303 computations of aerosol optical properties. ~~The parameter ranges for the bimodal size distribution~~
 304 ~~and mean complex refractive index of five aerosol subtypes are presented in Table 1 which are~~
 305 ~~used to construct the respective look-up tables (LUTs). These parameter values were adopted from~~
 306 ~~Dubovik, (2002); Torres et al., (2017) and Veselovskii et al., (2004), who used measurements from~~
 307 ~~sun-sky radiometers at multiple AEROSOL ROBOTIC NETWORK (AERONET) sites. Torres et al.,~~
 308 ~~(2017), validated their models against 744 AERONET observations and 165 almucantar~~
 309 ~~AERONET standard inversions at eight different sites. This approach ensures the robustness and~~
 310 ~~reliability of our aerosol characterization. The PSDs are given in terms of the total particle number~~
 311 ~~concentration, effective radius (r), and geometric standard deviation individually for fine and~~
 312 ~~coarse modes. Considering the sensitivity limitation of lidar measurements, the range of radius for~~
 313 ~~the PSD is constrained to 0.01-10 μm with a fixed bin size of 0.002 defined on a logarithmic-~~
 314 ~~equidistant scale in the calculation. In the process of constructing LUTs, specific intervals for the~~
 315 ~~parameters, σ_f , σ_c , r_f and r_c have been carefully chosen to define the range of particle size~~
 316 ~~distributions for each aerosol model. These intervals are set at 0.01, 0.01, 0.002 and 0.01 μm ,~~
 317 ~~respectively. These intervals are set as a compromise between accuracy and computation time,~~
 318 ~~ensuring that the LUTs encompass a comprehensive range of particle size distributions for various~~
 319 ~~aerosol subtypes found in the real atmosphere. Further details on the parameterization of the~~
 320 ~~bimodal particle size distribution is discussed in the subsequent section.~~

3.1.1 Lognormal Aerosol Size Distributions

322 An earlier study by [Kolmogorov, \(1941\)](#) mathematically proved that the random process of
 323 sequential particle crushing leads to a lognormal distribution of particle size. In our study, PSDs
 324 have been treated as a bimodal lognormal distribution, as widely used in aerosol remote sensing
 325 studies ([Dubovik et al., 2011](#); [Remer et al., 2005](#); [Schuster et al., 2006](#); [Torres et al., 2014](#)).
 326 Although particle size distributions are not always bimodal in each case, their size distributions
 327 can be considered as a combination of fine and coarse modes. This bimodal lognormal size
 328 distribution can be expressed as:

$$\frac{dn(r)}{d \ln(r)} = \sum_{i=1}^n \frac{N_{ti}}{(2\pi)^{1/2} \ln \sigma_i} \exp \left[-\frac{(\ln r - \ln r_i^n)^2}{2(\ln \sigma_i)^2} \right] \quad (1)$$

329 where N_{ti} is the total particle concentration of the i^{th} mode and r_i^n is the median radius for the
 330 aerosol size distribution, with n representing the number concentration distribution. The index $i =$

Deleted: Bi et al., 2009; Yang et al., 2007)

Deleted: Dubovik et al., (2006)

Deleted: The range of PSDs in the LUTs is sufficiently broad to cover realistic values for atmospheric aerosols

Deleted: Dubovik, (2002); Torres et al., (2017)

Moved down [1]: The PSDs are given in terms of the total particle number concentration, effective radius (r), and geometric standard deviation individually for fine and coarse modes.

Deleted: The parameters of bimodal distribution for five aerosol subtypes are derived using the measurements from sun/sky radiometer at multiple selected Aerosol Robotic Network (AERONET) sites .

Deleted:

Deleted: Torres et al., (2017)

Moved (insertion) [1]

Deleted: Table S1 lists the parameters of the bimodal lognormal PSDs and complex refractive index that were used for the construction of LUTs.

Deleted: In the calculations

Deleted: The

Deleted: of

Deleted: are f

Deleted: ixed

Deleted: .

Deleted: The

Deleted: following

Deleted: Kolmogorov, (1941)

358 f, c refers to the fine and coarse modes, respectively. The term $\ln \sigma_i$ is the mode width of the i^{th}
359 mode. This general bimodal lognormal size distribution shape for aerosol is adopted in this study
360 to improve the accuracy of the CCN retrieval. The sensitivity assessment regarding the response
361 of CCN to the assumption of bimodal size distributions is presented in section 3.1. For individual
362 lognormal components, the relationships between the volume and number distribution parameters
363 representing by the following equations (Hatch & Choate, 1929);

$$r^n = r^v / \exp[3(\ln \sigma)^2] \quad (2)$$

$$V_t = N_t \frac{4\pi}{3} (r^n)^3 \exp\left[\frac{9}{2}(\ln \sigma)^2\right] \quad (3)$$

364 where, V_t is the particle volume concentration and r^v is the median radius for the aerosol volume
365 size distribution. As shown in Figure 1 and Table 1, the main difference between the aerosol
366 subtype is the ratio of the volume concentration of the fine mode to the coarse mode.

367 3.2 Retrieval of CCN Number Concentrations

368 Building upon the methodology proposed by (Lv et al., 2018), we have enhanced and
369 generalized the approach to enable its application to airborne and spaceborne lidar measurements
370 for CCN estimation. The core of the algorithm relies on the utilization of look-up tables (LUTs)
371 that incorporate aerosol size and composition information, facilitating reliable and vertically-
372 resolved CCN estimation. N_{CCN} values are obtained at six critical supersaturations from 0.07% to
373 1.0% based on retrieved particle size distributions. Significant improvements have been
374 implemented within the methodology. Firstly, its applicability has been expanded to accommodate
375 lidar measurements from diverse platforms. Secondly, the LUTs now include five aerosol types,
376 ensuring a more comprehensive representation of aerosol characteristics. Thirdly, the methodology
377 leverages the additional signal of the extinction coefficient at 1064 nm, effectively addressing the
378 uncertainty associated with the non-uniqueness problem during the inversion process. Fourthly,
379 including the hygroscopic growth correction in the revised method has led to significant
380 improvements in the accuracy of CCN estimation, further enhancing the reliability and robustness
381 of the. Finally, results the extensive analysis has been conducted by including the errors from RH.

382 This section discusses a detailed methodology adopted by ECLiAP to retrieve N_{CCN} from
383 the given lidar measurements.

384 3.2.1 Overview

385 An optically related N_{CCN} is introduced to bridge the gap between aerosol particle and their
386 activation capability to serve as a cloud droplet. The ability of particles to act as CCN is mainly
387 controlled by particle size distribution followed by chemical composition (Dusek et al., 2006; Patel
388 & Jiang, 2021). However, both factors are significant in specific regions (Mamouri & Ansmann,
389 2016, 2016). Therefore, N_{CCN} could be quantified with size distribution and compositional

Deleted: (Hatch & Choate, 1929)

Deleted: S

Deleted: (Lv et al., 2018)

Formatted: Indent: First line: 0.4"

Deleted: (Dusek et al., 2006; Patel & Jiang, 2021)

Deleted: and meteorological conditions

Deleted: (Mamouri & Ansmann, 2016)

396 information. The key feature of an approach adopted in ECLiAP is to seek the parameters that can
397 provide the size and composition of particles consistent with lidar measurements under dry
398 conditions and use these parameters to estimate N_{CCN} .

399 Figure 2 illustrates a schematic diagram of the method to retrieve N_{CCN} from satellite observations.

400 In the natural environment, the particle hygroscopic properties influence the particle size
401 distribution and their optical properties, especially when it is near a cloud base or under a high
402 moist environment. Therefore, the lidar measured aerosol optical properties under ambient
403 conditions need to be corrected to the dry aerosol optical properties using the hygroscopic
404 enhancement factor. The hygroscopic enhancement factor can be fitted by the parameterization
405 scheme using enhancement of backscatter and extinction coefficients with RH. Particle dry
406 backscatter and extinction can also be inferred from the hygroscopic enhancement factor. An
407 approach to computing hygroscopic enhancement factors and performing hygroscopic correction
408 to obtain dry backscatter and extinction is described in Section 2.2.2. This step is applied to all the
409 $3\beta+3\alpha$ parameters before looking for aerosol size parameters from the LUT. Before applying
410 hygroscopic correction, lidar-measured optical properties, particularly for dust mixture (polluted
411 dust and dusty marine), are separated into dust and non-dust components using the backscatter
412 coefficients and particle depolarization ratio (Tesche et al., 2009). The methodology to separate
413 the dust mixture is discussed in Appendix A1. The resulting dust and non-dust aerosol optical
414 properties, along with aerosol subtype and relative humidity, is then utilized in the ECLiAP
415 algorithm (as shown in Figure 2) to estimate CCN concentrations. Note that the direct inclusion of
416 internal mixtures in our analysis and LUTs poses complexity and challenges. As a result, our
417 approach primarily centers on studying and analyzing external mixtures of aerosol subtypes.

418 Once the dry aerosol optical properties are derived, an ECLiAP look for the suitable size
419 parameters from the LUTs for the given dry aerosol optical properties and respective aerosol
420 subtype (see section 2.2.3). As mentioned earlier, the ability of particles to act as CCN is mainly
421 controlled by particle size distribution followed by chemical composition. Deriving composition
422 information of particles from the lidar measurements is not yet well-defined. Therefore, in the
423 absence of chemical composition data, mean chemical composition information denoted by a
424 single value of κ , the so-called hygroscopicity parameter, is achievable for estimating N_{CCN} , which
425 describes the relationship between the particle dry diameter and CCN activity. The sensitivity of
426 the estimated N_{CCN} to κ depends strongly on the variability of the shape of the aerosol size
427 distribution (Wang et al., 2018). Therefore, the chemical information becomes less important in
428 estimating N_{CCN} , especially (Patel & Jiang, 2021) (Jiang, 2021). Most studies reported that the
429 uncertainty of using the mean value of κ to estimate the N_{CCN} is less than 10% (Jurányi et al., 2010;
430 Wang et al., 2018), which varies with atmospheric conditions. In ECLiAP, the literature values of
431 κ are considered for each aerosol subtype for further retrieval. The κ is assumed to be 0.7 for
432 marine (Andreae & Rosenfeld, 2008), 0.03 for dust (Koehler et al., 2009), 0.27 for polluted
433 continental (Liu et al., 2011), 0.3 for clean continental (Andreae & Rosenfeld, 2008), and 0.1 for
434 smoke aerosols (Petters et al., 2009) for the later computations.

Deleted: mixture

Deleted: (Tesche et al., 2009)

Deleted: (Wang et al., 2018)

Deleted: ally at higher supersaturation

Deleted: (Patel & Jiang, 2021)

Deleted: (Jurányi et al., 2010; Wang et al., 2018)

Deleted: (Andreae & Rosenfeld, 2008)

Deleted: (Koehler et al., 2009)

Deleted: (Liu et al., 2011)

Deleted: (Andreae & Rosenfeld, 2008)

Deleted: (Petters et al., 2009)

446 Finally, an ECLiAP uses the retrieved optically equivalent size parameters from LUTs and κ value
447 as composition information for the further computation of critical radius using the κ -Köhler theory
448 (Petters & Kreidenweis, 2007), and hence the N_{CCN} for the six fixed supersaturations (see section
449 2.2.4). For the dust mixture, N_{CCN} derived separately both for dust and non-dust are added lastly.

Deleted: (Petters & Kreidenweis, 2007),

450 3.2.2 Separation of optical properties for dust mixture

Formatted: Font: Bold

Formatted: Heading 3

451 We have adopted the methodology by Tesche et al., (2009) to separate the dust and non-
452 dust extinction coefficients in the dust mixtures (polluted dust and dusty marine) using particle
453 backscatter coefficients and particle depolarization ratio. The optical properties

$$\beta_a = \beta_p \frac{(\delta_p - \delta_2)(1 + \delta_1)}{(\delta_1 - \delta_2)(1 + \delta_p)} \quad (A1.1)$$

454 This study incorporates wavelength-dependent depolarization ratios δ_1 and δ_2 to distinguish the
455 dust and non-dust aerosol components. The reported particle depolarization ratio from various
456 campaigns is listed in the Table S1. In this study, mean values of δ_1 (0.24, 0.31 and 0.06) and δ_2
457 (0.03, 0.05, and 0.02) at 355, 532 and 1064 nm, respectively, are utilized. If the measured
458 depolarization ratio $\delta_p \geq \delta_1$ ($< \delta_2$) then aerosol mixture is considered as pure dust (non-dust). For
459 remaining δ_p values, we first estimate β_a using the above equation and then calculate β_{nd} by
460 subtracting β_a from β_p . Subsequently, the extinction coefficients are computed by multiplying the
461 backscatter coefficients with the respective lidar ratio. Determining a spatially varying lidar ratio
462 for dust across different regions presents challenges due to uncertainties in identifying dust source
463 regions during transport. Therefore, we employ a simplified approach using a single lidar ratio
464 value. Previous studies have reported little to no wavelength dependency of lidar ratio for dust and
465 marine aerosol based on ground-based Raman lidar and airborne HSRL lidar measurements. As a
466 result, we consider a constant lidar ratio of 44 for dust and 23 for marine to calculate the extinction
467 coefficients at the three wavelengths. However, for polluted continental aerosols, we utilize
468 wavelength-dependent lidar ratios of 58, 70 and 30 at 355, 532 and 1064 nm (Giannakaki et al.,
469 2016; Hänel et al., 2012; Kim et al., 2018; Komppula et al., 2012; Müller et al., 2007).

Formatted: Normal, Space After: 0 pt, Line spacing: single

Deleted: (Giannakaki et al., 2016; Hänel et al., 2012; Kim et al., 2018; Komppula et al., 2012; Müller et al., 2007)

470 3.2.3 Derivation of dry backscatter and dry extinction

471 It is difficult to measure the complex chemical composition and associated water uptake capability
472 of a particle with increasing RH. Therefore, a widely popular and simple parameterization scheme
473 was used to describe the changes in aerosol optical properties with atmospheric RH relative to a
474 dry (or low-RH) state, also called the hygroscopic enhancement factor. Recent aerosol hygroscopic
475 studies (Bedoya-Velásquez et al., 2018; Fernández et al., 2018; Lv et al., 2017), have derived
476 backscatter and extinction enhancement factors using lidar measurements and RH profiles. The
477 hygroscopic enhancement factor that is associated with both particle size and hygroscopicity
478 (Kuang et al., 2017), is defined as:

Deleted: (Bedoya-Velásquez et al., 2018; Fernández et al., 2018; Lv et al., 2017)

Deleted: (Kuang et al., 2017)

$$f_{\xi}(RH, \lambda) = \frac{\xi(RH, \lambda)}{\xi(RH_{dry}, \lambda)} \quad (4)$$

485 where f_{ξ} is the hygroscopic enhancement factor of the optical property ξ (backscatter and
 486 extinction) at a specific light wavelength λ and RH, and RH_{dry} is the reference RH value (RH=0).
 487 There is no generic reference RH that represents the dry conditions for lidar measurements, unlike
 488 in-situ controlled RH measurements, to derive enhancements factor. Inferring dry backscatter and
 489 extinction coefficients is also crucial in CCN retrieval. Therefore, parameterization of the
 490 hygroscopic growth of lidar-derived optical properties should combine dry aerosol optical
 491 properties and $f_{\xi}(RH, \lambda)$ together. Previous studies have proposed several parameterization
 492 schemes for hygroscopic enhancement factors (Titos et al., 2016). The most frequently used
 493 parameterization scheme is a power-law function that is known as gamma parameterization,
 494 introduced by Kasten, (1969):

$$f_{\xi}(RH, \lambda) = A \cdot (1 - RH/100)^{-\gamma} \quad (5)$$

495 Where the parameter A gives the extrapolated value at RH=0% and the exponent γ is the fitting
 496 parameter and defines the hygroscopic behavior of the particles. Recently, a new physically based
 497 single-parameter representation approach was proposed by Brock et al., (2016), to describe the
 498 hygroscopic enhancement factor. Their results claimed that this proposed parameterization scheme
 499 better describes light-scattering hygroscopic enhancement factors than the widely used gamma
 500 power-law approximation. The formula of this new scheme is written as:

$$\xi(RH, \lambda) = \xi_{dry}(RH, \lambda) \cdot f_{\xi}(RH) = \xi_{dry}(RH, \lambda) \cdot \left[1 + \kappa_{\xi}(\lambda) \frac{RH}{100 - RH} \right] \quad (6)$$

501 where, κ_{ξ} is a dimensionless fitting parameter and shows a significant correlation with bulk
 502 hygroscopic parameter κ ; but they are not equivalent (Brock et al., 2016; Kuang et al., 2017). ξ_{dry}
 503 denotes dry aerosol optical properties (backscatter and extinction coefficients).

504 For the estimation of the hygroscopic enactment factor, aerosol optical properties (backscatter and
 505 extinction coefficients) at 355, 532, and 1064 nm are calculated over a range of RH (0-99%) using
 506 Mie theory (T-matrix and IGOM for spheroid) for the range of PSDs and each aerosols subtype.
 507 Figure S1 illustrates the mean curve of the hygroscopic enhancement factor (the ratio between the
 508 aerosol optical properties at specific RH to dry RH) at three wavelengths with increasing RH for
 509 each aerosol subtype. With given aerosol optical properties at different RHs, κ_{ξ} can be fitted by
 510 curve fitting using Eq. (6). However, Tan et al., (2019), based on a comparison of κ_{ξ} and derived
 511 ξ_{dry} for various ranges of RH, showed that the fitting hygroscopic parameters are found to be
 512 sensitive to fitting RH range when the RH range is limited and relatively high (between 60% and
 513 90%). Therefore, we fixed the RH range to 60%-90% for the parameter fitting (highlighted curve
 514 in Figure S1). In addition, retrieving finite dry aerosol optical properties could not be possible for

Deleted: (Titos et al., 2016)

Deleted: Kasten, (1969)

Deleted: Brock et al., (2016)

Deleted: performs better in describing

Deleted: (Brock et al., 2016; Kuang et al., 2017)

Deleted: Tan et al., (2019)

521 the observation with RH > 99%. Therefore, ECLiAP only applies the hygroscopic correction when
 522 RH is between 40% and 99%. In ECLiAP, individual κ_{ξ} values for each aerosol optical property
 523 at three different wavelengths, along with the RH value, are used to obtain the dry aerosol optical
 524 properties separately for each aerosol subtype using Eq. (6).

525 3.2.4 Inversion techniques for size parameters

526 ECLiAP utilizes an inverse approach, distinct from traditional methods, to estimate the particle
 527 size distribution from Look-Up Tables (LUTs) using lidar inputs. This process involves inferring
 528 particle size distribution from known aerosol optical properties, determining the best-fitting
 529 solution that corresponds to the observed lidar measurements. It differs from the traditional $3\alpha+2\beta$
 530 technique typically used for inversion.

531 Once the dry aerosol optical properties are obtained, the ECLiAP searches for suitable size
 532 parameters from the LUTs. For this, the ECLiAP look for the best combination of six values (N_{if} ,
 533 r_f , σ_f , N_{ic} , r_c , σ_c) to match inputs (β_{355} , β_{532} , β_{1064} , α_{355} , α_{532} , α_{1064}) by minimizing the following
 534 function:

$$\mu^{sum} = \sum_{i=1,2,6} \left| \frac{x_i - x'_i}{x_i} \right| \quad (7)$$

535 Where x_i represents input aerosol optical data (β_{355} , β_{532} , β_{1064} , α_{355} , α_{532} , α_{1064}) and x'_i is aerosol
 536 optical data (β'_{355} , β'_{532} , β'_{1064} , α'_{355} , α'_{532} , α'_{1064}) derived from LUTs, which are calculated from
 537 Mie theory (or T-matrix and IGOM for spheroid) and size distribution parameters.

538 Each LUT consists of two parts to reduce the dimensions and size of LUTs. Therefore, the particle
 539 size distribution, as shown in Eq. (1), can be rewritten as:

$$\frac{dn(r)}{d \ln(r)} = \sum_{i=f,c} \left\{ \frac{1}{(2\pi)^{1/2} \ln \sigma_i} \exp \left[-\frac{(\ln r - \ln r_i^n)^2}{2(\ln \sigma_i)^2} \right] \cdot N_{ti} \right\} = \sum_{i=f,c} x_i \cdot N_{ti} \quad (8)$$

540 Where x_f and x_c refer to the data bank precomputed with (σ_f, r_f and r) and (σ_c, r_c and r),
 541 respectively. Furthermore, we have adopted the successive approximation method (Kantorovitch,
 542 1939) to deal with the extensive range of N_{tf} and speed up the finding for the closest solution.
 543 Therefore, the inversion technique is further divided into two steps. Step-1: search for an
 544 approximate solution based on the criterion in Eq. 8 and calculate the corresponding aerosol optical
 545 data (β'_{355} , β'_{532} , β'_{1064} , α'_{355} , α'_{532} , α'_{1064}) from the data banks (x_f and x_c) and N_{tf} and N_{tc} . The step
 546 widths of N_{tf} and N_{tc} are considered to be 100 and 0.1 cm^{-3} , respectively. Step 2: based on the
 547 approximate solution obtained in step 1, determine the smallest solution space of N_{tf} by repeating
 548 the procedure in step 1 using a smaller step width of 10 cm^{-3} for N_{tf} . Search for the optimal solution
 549 of six size parameters (N_{if} , r_f , σ_f , N_{ic} , r_c , σ_c).

Deleted: the

Deleted: (Kantorovitch, 1939)

552 3.2.5 Estimation of N_{CCN}

553 For the given aerosol optical properties, the retrieved size parameters and the associated
554 hygroscopicity parameter (κ ; as discussed in section 2.2.1) were used to calculate the critical
555 radius. The critical radius (r_{crit}) above which all particles are activated into droplets for a certain
556 supersaturation ratio (S_c) can be computed from the κ -Köhler theory as suggested by [Petters &](#)
557 [Kreidenweis, \(2007\)](#);

$$D_{crit} = \left(\frac{4A^3}{27 * \kappa * \ln(S_c)^2} \right)^{1/3}; \quad A = \frac{4\sigma_{s/a}M_w}{RT\rho_w} \quad (9)$$

558 Where, D_{crit} is the critical diameter ($r_{crit} = D_{crit}/2$), and $S_c = SS + 1$, M_w and ρ_w are the
559 molecular weight and water density, while R and T are the ideal gas constant and the absolute
560 temperature, respectively and $\sigma_{s/a} = 0.072 \text{ J m}^{-2}$. The critical radius is determined at six critical
561 supersaturations for activation (0.07%, 0.1%, 0.2%, 0.4%, 0.8% and 1.0%). [While lidar](#)
562 [measurements are more sensitive to particles with sizes around 50 nm and larger, this method](#)
563 [incorporates factors such as particle size distribution, chemical composition, supersaturation](#)
564 [levels, and thermodynamic properties to estimate the critical radius even for particles below the](#)
565 [typical lidar sensitivity range.](#)

566 Finally, the ECLiAP calculates N_{CCN} by integrating size distribution from critical radius to
567 maximum radius as:

$$N_{ccn} = \int_{\ln r_c}^{\ln r_{max}} \frac{dn(r)}{d \ln(r)} d \ln(r) \quad (10)$$

568

569 **4 Results**

570 **4.1 Sensitivity analysis**

571 Evaluating the algorithm is a challenging task in the absence of standard and reliable
572 measurements. The performance of the ECLiAP is evaluated using numerically simulated
573 observations with different error characteristics.

574 **4.1.1 Retrieval of N_{CCN} with error-free data**

575 [To assess the inversion performance and stability ECLiAP, we first performed a sensitivity](#)
576 [analysis under the assumption of error-free lidar measurements. We used 2000 different sets of](#)
577 [bimodal size distributions for each aerosol subtypes and used them to simulate the lidar](#)
578 [observations. The retrieval was repeated to each simulated lidar observations, and the retrieved](#)

Deleted: Petters & Kreidenweis, (2007)

580 size parameters were used to calculate the errors in the retrieved N_{CCN} (N_{CCN}^{ret}) with respect to the
581 initial inputs (N_{CCN}^{int}). The errors were calculated as the percentage difference using Eq. 8.

$$CCN\ Error = [(N_{CCN}^{ret} - N_{CCN}^{int})/N_{CCN}^{int}] \times 100\% \quad (11)$$

582 Table 2 lists the statistical results of CCN error for each aerosol type. As the number shows, the
583 initial N_{CCN} is well reproduced from the error-free inputs for each aerosol size distribution. The
584 standard deviation of the retrieved CCN errors from the different sets of bimodal size distribution
585 data is also estimated along with the mean value to determine the range of the retrieved CCN error.
586 As mentioned above, the appropriate balance between the accuracy and processing time of the
587 LUTs leads the mean CCN error close to zero but not equal to zero. However, the small standard
588 deviation (<0.25) indicates the smaller variances of errors among the aerosol size distributions.
589 Although the high accuracy of LUTs provides the CCN error closer to zero, the calculations are
590 more time expensive. In general, the retrieval results shown in Table 2 exhibit the good accuracy
591 and stability of the inversion algorithm for each aerosol subtype.

592 Additionally, the sensitivity of the N_{CCN} retrieval to the assumption of the bimodal size distribution
593 is tested against the aerosol size distribution measurements at the U.S Department of Energy's
594 Atmospheric Radiation Measurement (ARM) climate research facility from the Southern Great
595 Plain (SGP) site. Particle size distribution was measured simultaneously by an Ultra-High
596 Sensitivity Aerosol Spectrometer (for the 0.07 to 1 μm geometric diameter range) and an
597 Aerodynamic Particle Sizer (TSI-3321; for the 0.7 to 5 μm aerodynamics diameter range). The
598 size conversion factor, defined as the ratio of aerodynamic diameter to geometric diameter, was
599 used to construct a trimodal lognormal particle size distribution. For the purpose of this study, the
600 corresponding bimodal fits are produced, which are representative of the observed size
601 distributions. Figure S2 shows an example of the observed aerosol size distribution and the
602 corresponding bimodal fits. The comparison suggests that bimodal lognormal size distributions
603 can well represent the observed aerosol size distributions qualitatively. Later, we calculate N_{CCN}
604 based on the bimodal fits and compare them with the 100 observed size distributions to quantify
605 the errors arising from the bimodal lognormal fits. The associated κ values are estimated based on
606 observed PSDs and N_{CCN} values as described in Patel & Jiang, (2021). The induced CCN errors
607 from the bimodal fitting are shown in Table 3. The absolute value of N_{CCN} retrieval errors is 3.9%,
608 with a standard deviation of 2.8% at 0.1% supersaturation. Overall, the results suggest that bimodal
609 lognormal aerosol size distributions are adequate for retrieving N_{CCN} , but errors from the bimodal
610 assumption are not negligible.

611 4.1.2 Impact of systematic and random errors on N_{CCN} retrieval

612 Both systematic and random errors exist in lidar-retrieved measurements (Mattis et al., 2016).
613 Systematic errors can be induced by experimental conditions, retrieval algorithms, data processing
614 methods, and our understanding of physical interactions. Sensitivity analysis tests the impacts of
615 systematic errors from backscatter and extinction coefficients on N_{CCN} retrieval. Although the

Formatted: Subscript

Deleted: Firstly, error-free lidar measurements are considered as inputs to evaluate the inversion stability of ECLiAP. The retrieval procedure is repeated for 2000 different sets of the bimodal size distribution for each aerosol type. Errors are calculated in retrieved N_{CCN} (N_{CCN}^{ret}) with respect to the initial inputs (N_{CCN}^{int}) using Eq. 8.

Formatted: Font:

Deleted: 1

Deleted: are

Deleted: 1

Deleted: Patel & Jiang, (2021)

Deleted: 2

Deleted: (Mattis et al., 2016)

628 systematic errors of different parameters are correlated, the errors are considered independent for
629 individual lidar measurements in the simulations. The error range is reasonable for most current
630 lidar systems. The systematic errors ranging from -20% to 20% with an interval of 5% are applied
631 to one input parameter at a time (others are kept error-free) in each test to understand the impacts
632 on individual parameters better. The inversion algorithm is performed to obtain a new set of aerosol
633 size distributions and retrieve N_{CCN} data. The procedure is repeated for each input parameter and
634 error value with 200 sets of the randomly generated size distribution for each aerosol subtype. The
635 percentage errors in N_{CCN} associated with systematic errors can be estimated by comparing
636 retrieved and initial values of N_{CCN} using Eq. 11. Note that we have also conducted additional
637 simulations for higher range of the error and found that our results are unchanged. However, Pérez-
638 Ramírez et al., (2013) demonstrated that larger errors in the input data can cause significant and
639 unpredictable deviation in the retrieved results. The error range $\pm 20\%$ is reasonable for most lidar
640 systems.

641 Figure 3 illustrates the error in retrieved N_{CCN} as a function of the systematic errors in backscatter
642 and extinction coefficients. The slope of the curve indicates the sensitivity of N_{CCN} errors to
643 systematic errors in individual parameters. A steeper slope infers a high sensitivity in the N_{CCN}
644 retrieval to the systematic error for a given input parameter. Errors in retrieved N_{CCN} increase as
645 errors of backscatter and extinction increase, and it is even steeper at higher supersaturations. In
646 general, N_{CCN} retrievals are most sensitive to errors in extinction coefficients followed by
647 backscatter coefficients. Interestingly, the results are less sensitive to errors in backscatter
648 coefficients at lower supersaturations ($\leq 0.2\%$) but are relatively more sensitive at higher
649 supersaturations ($> 0.2\%$). This indicates that reducing uncertainties in the extinction coefficients
650 can effectively improve the accuracy of N_{CCN} retrieval while reducing uncertainty in backscatter
651 coefficients can be beneficial for retrieving N_{CCN} at higher supersaturation. Errors in α_{355}
652 influence the retrieval results the most. On average, a positive relative error of 20% in α_{355}
653 overestimates the N_{CCN} retrieval by about 20% at lower supersaturation and about 50% at higher
654 supersaturation. A negative error of 20% in α_{355} underestimates the N_{CCN} retrieval, and the degree
655 of impact is slightly higher than the positive error. Errors in α_{532} and α_{355} have the opposite effect
656 on the retrieval error. It is also clear that the influence of systematic errors on the retrieval of N_{CCN}
657 varies with activation radius, as elucidated by the different signs of the slopes. For instance, the
658 slopes of the extinction coefficient for dust aerosols reverse the sign when the activation radius
659 exceeds low to high supersaturation. These differences most likely result from the reduced retrieval
660 sensitivity to the coarse mode of the aerosol size distribution. In addition, there are substantial
661 distinctions among the types of aerosols. Dust and marine aerosols have the largest absolute errors
662 compared to others dominated by fine-mode particles (see Table 2). These collectively indicate
663 that there are better constraints for fine-mode aerosols than for coarse-mode aerosols, which
664 introduce a larger retrieval error in N_{CCN} for aerosols with more weight in the coarse mode. It is
665 noteworthy that incorporating an additional input signal of extinction coefficient at 1064 nm in the
666 ECLiAP reduces the error by $\sim 20\%$ in the coarse mode-dominated aerosol subtypes (dust and
667 marine), and $\sim 15\%$ in total compared to the previous studies (Lv et al., 2018; Tan et al., 2019).

Deleted: distribution

Formatted: Font color: Black

Deleted: ¶

Deleted: the

Formatted: Subscript

Deleted: an

Formatted: Subscript

Formatted: Subscript

Deleted: fine mode

Deleted: 1

Deleted: fine mode

Deleted: coarse mode

676 Nevertheless, integrating an additional lidar signal at a wavelength longer than 1064 nm may
677 further reduce retrieval error for the coarse mode-dominated aerosol type.

678 RH is another crucial parameter in the present retrieval algorithm for N_{CCN} . Errors in RH derived
679 by remote-sensing or reanalysis influence the values of growth factors and result in the dry aerosol
680 optical properties, which in turn influence all the input parameters. Therefore, systematic errors
681 ranging from -10% to 10% in intervals of 2% are considered for RH. Figure 4 shows the result of
682 systematic errors in RH. We observed that N_{CCN} is overestimated when RH has a negative
683 systematic error, and the extent of overestimation in N_{CCN} increases as the error increase. A
684 negative error of 10% in RH overestimates N_{CCN} at lower supersaturation by about 20% and
685 doubles (~40%) at higher supersaturation. The effects of the positive errors in RH are relatively
686 smaller and more complicated than negative errors. The mean retrieval error peaked at the RH
687 error at 6%, and the standard deviation of retrieval error increased with the RH error. This suggests
688 that underestimating RH causes large errors than overestimation. Therefore, extra care should be
689 paid to RH measurements if RH-related hygroscopic enhancements of aerosol optical properties
690 are considered.

691 Systematic errors introduce mean biases in N_{CCN} retrievals, whereas random errors in observations
692 produce random N_{CCN} retrieval errors. Random errors obeying Gaussian distributions are produced
693 arbitrarily with a mean value of zero. The standard deviations are set to 10% for aerosol optical
694 properties and to 5%, 10%, and 20% for RH in each test. The simulation is repeated 5000 times
695 for each aerosol subtype, and the statistical results are presented in Figure 5. The mean values of
696 relative error are presented by color, and the number indicates the standard deviation. The error
697 does not change significantly as the random error of RH increases. The mean random errors are
698 relatively small and non-zero, mainly because the sensitivities of N_{CCN} retrievals are different for
699 different aerosol optical data. The standard deviations are within 16%-28%. The results reveal that
700 random errors in the given input parameters may also contribute to systematic errors in the N_{CCN}
701 retrievals. The largest mean relative errors are found for coarse mode-dominated aerosol subtypes
702 (dust and marine), consistent with the sensitivities to systematic errors. As discussed earlier,
703 considering additional lidar measurements at longer wavelengths that are more sensitive to larger
704 particles could improve the retrieval of N_{CCN} for the coarse mode-dominated aerosol subtypes. The
705 mean values of relative errors increase with increasing supersaturation for all aerosol types. Errors
706 in the retrieved N_{CCN} follow a Gaussian distribution for low supersaturation. However, the
707 Gaussian shape disappears, and the high frequencies shift to the edge of the distribution when
708 supersaturation shifts from low to high (not shown here). Furthermore, the influence of random
709 errors on the individual input parameters is also assessed and is shown in Figure S3. Random errors
710 underestimate the enhancement factor (κ_{ξ}) by 30%-40% for 5% RH error, 45%-60% for 10% RH
711 error, and 65%-75% for 20% RH error. The relative errors in β are likely to be overestimated,
712 whereas they are underestimated in α . The absolute relative error of input parameters becomes
713 larger as the random error of RH grows.

Deleted: the

Deleted: the

Deleted: the

717 4.2 Comparison with airborne measurements

718 The evaluation of N_{CCN} retrieval depends on how well retrieved and observed values are matched,
719 as matching errors can become overwhelming. Therefore, we have carried out a validation
720 approach by comparing ECLiAP retrieved N_{CCN} from lidar measurements with the in-situ
721 measurements of N_{CCN} by CCN counter during the NASA ORACLES airborne campaign, which
722 occurred from 2016 to 2018 over the Southeast Atlantic (SEA) (Redemann et al., 2021; Zuidema
723 et al., 2016).

724 HSRL-2 measures the vertical profiles of aerosol optical properties, whereas the CCN counter
725 provides measurements for point location. Therefore, we carried out two strategically different
726 validation exercises in this study: (1) the vertical profile-based comparison and (2) the comparison
727 of collocated measurements. For the profile-based comparison, an ascending path of flight (area
728 covered within the yellow dashed line in Figure S4) on 19 October 2018 has been considered, so
729 the measurements of the CCN counter can be available at various altitudes. Prior to comparison,
730 the lidar measurements from HSRL-2 are averaged over a selected wide space and time (yellow
731 dashed line box in Figure S4). The N_{CCN} measurements from the CCN counter were available at
732 the supersaturation between 0.32% and 0.34%. Hence, the N_{CCN} were retrieved at the
733 supersaturation of 0.34% by applying ECLiAP to the mean profiles of lidar measurements. It is
734 noteworthy that the retrieval has been carried out only on those observations having valid lidar
735 measurements at least for two wavelengths. Figure 6a demonstrates the retrieval fit to HSRL-2's
736 vertical dry aerosol extinction coefficient measurements at 355, 532, and 1064 nm. A smoke
737 aerosol dominates the ~93% of profiles at the altitude above 800 meters and marine at lower
738 altitudes (< 800 m), having RH between 30%-105%. The finite dry aerosol optical properties close
739 to the surface could not be retrieved for the observations with RH>99%. The retrieved profiles of
740 dry extinction coefficients are in better agreement with the measured by HSRL-2. This illustrates
741 the ability of the kappa parametrization to account for aerosol hygroscopicity. The vertical mean
742 of absolute fitting error of extinction coefficient is found to be 3.2%, 4.8%, and 6.3% for 355, 532,
743 and 1064 nm, respectively, and the vertical mean of absolute fitting error of backscatter
744 coefficients is 5.1%, 6.7% and 8.9% for 355, 532 and 1064 nm respectively. The fit to the
745 backscatter coefficients of 1064 nm has a relatively larger error. Certainly, one needs to know that
746 the vertically resolved extinction coefficient at 1064 nm is derived using the backscatter coefficient
747 at 1064 nm and lidar ratio. Since HSRL-2 does not directly measure extinction at 1064 nm, it is
748 computed from an assumed relationship with the measured lidar ratio at 532 nm. Though provided
749 as a best guess, such an estimate may cause extra uncertainty to the 1064 nm. Furthermore, the
750 comparison of vertical profiles of ECLiAP retrieved N_{CCN} from lidar measurements and the N_{CCN}
751 measured by the CCN counter is shown in Figure 6b. The retrieved values captured the pattern of
752 altitude variations in N_{CCN} as observed by the in-situ measurements. However, the magnitude of
753 retrieved N_{CCN} is slightly overestimated by ~12% in total. The overestimation is lower (~9%) at
754 above 2 km, whereas, at below 1 km, it is slightly higher (~16%). A plausible reason behind the
755 relatively large overestimation at below 1 km might be the considerable variation of RH between
756 60%-105% or/and the highly variable aerosol properties due to the mixture of multiple aerosol

Deleted: Observations of Aerosols above Clouds and their interactions (...)

Deleted:)

Deleted: (Redemann et al., 2021; Zuidema et al., 2016)

Deleted: The ORACLES data contain measured in-situ N_{CCN} from the CCN counter and lidar measurements with NASA Langley Research Center's high-spectral resolution lidar (HSRL-2). We took the opportunity to conduct the validation exercise based on the accessible data.

Deleted: demonstrated

Deleted: coefficients

Deleted: Furthermore, the

769 subtypes (smoke, marine, and dust). In addition, wind-driven advection and the age of the air parcel
770 radically modify the characteristics of smoke aerosols and their hygroscopic behavior, which also
771 leads to the slight overestimation of retrieved N_{CCN} values. The discrepancy between the retrieved
772 and observed values of N_{CCN} should be reassessed with the robust measurements from the varieties
773 of aerosol subtypes using the multi-campaign airborne data.

774 The second robust validation exercise is performed, based on collocated measurements,
775 using two years (2017-2018) of combined data from the ORACLES campaign. In 2017-2018, both
776 HSRL-2 and CCN counter were installed on the NASA P-3 flight. The end goal of this exercise is
777 to find one lidar measurement from HSRL-2 to directly compare with one N_{CCN} measured by the
778 CCN counter, both observed in approximately the same time and space. We defined collocation
779 criteria for any given HSRL-2 profile as follows. The collocation method finds CCN measurement
780 that falls within ± 1.1 km horizontal distance, ± 60 m vertical distance, and ± 10 minutes of the time
781 window. Later, the meteorological parameters within the given space and time windows are
782 extracted along with lidar measurements and measured N_{CCN} from each flight of the 2017-2018
783 ORACLES campaign. ECLiAP is applied to each lidar measurement for N_{CCN} retrieval on the
784 same supersaturation value measured by the CCN counter (lies within the range from 0.2-0.4%
785 SS). Figure 7 represents the result from the comparison of retrieved and measured N_{CCN} . The N_{CCN}
786 inferred from the CCN counter measurement is in better agreement with the retrieved N_{CCN} with a
787 correlation coefficient (R) of ~ 0.89 , a root mean square error (RMSE) value of 302.8 cm^{-3} , and a
788 bias of 138.8 cm^{-3} . The systematic positive bias in the comparison indicates that the retrieved N_{CCN}
789 are overestimating the observed values. It is noteworthy that smoke aerosols dominate in the
790 observations from ORACLES, but it also has significant observations from marine, dust, and
791 polluted dust. The discrepancy between measured and retrieved values could be due to the
792 variabilities in the aerosol properties. Overall, the strong correlation in the validation results
793 demonstrates the potential of ECLiAP in retrieving N_{CCN} from lidar measurements. It recommends
794 having a detailed validation study separate for aerosol subtypes using ground-based and aircraft
795 measurements to evaluate the reliability of the ECLiAP algorithm in estimating the N_{CCN} .

796 4.3 Retrieving N_{CCN} from spaceborne lidar (CALIOP/CALIPSO): a case study

797 Extending the scope of ECLiAP, the methodology was converted into a procedure that can be
798 applied to any level-2 aerosol profile dataset from Cloud-Aerosol Lidar with Orthogonal
799 Polarization (CALIOP) on the Cloud-Aerosol Lidar and Infrared Pathfinder Satellite Observations
800 (CALIPSO) (Winker et al., 2007). As an illustrative example, this procedure was applied to a
801 regular CALIPSO track for 01 January 2019 starting at 20:08 UTC, which spans from 10°N to 40°N ,
802 passing over the Tibetan plateau and Indian landmass. The CALIPSO track (solid black line)
803 can be seen on the right-hand side in Figure 8a. CALIOP onboard CALIPSO provides
804 measurements of aerosol optical properties only at two wavelengths (532 and 1064 nm). Therefore,
805 a total of six parameters (β_{532} , β_{1064} , α_{532} , α_{1064} , depolarization ratio, and aerosol subtypes) from
806 CALIOP along with meteorological parameters (RH, temperature) are provided as the inputs to
807 ECLiAP and retrieved total particle concentration (N_{CN}) and N_{CCN} at six supersaturations as

808 outputs. The N_{CN} amount represents the total number of aerosol particles that can serve as centers
809 for condensation, while the N_{CCN} is the fraction of N_{CN} that can activate as CCN.

810 The extinction coefficient at 532 nm and aerosol subtypes, along with retrieved N_{CN} and N_{CCN} at
811 supersaturation of 0.4%, are shown in Figure 8. Unfortunately, due to the retrieval limitation over
812 the elevated region along with cloudiness, there are no valid aerosol measurements over the
813 Himalayan-Tibetan plateau (as shown by a gap between 28 °N to 37 °N). On the contrary, a strong
814 mixed aerosol signal is observed over the Indian landmass (α_{532} larger than 2.5 km⁻¹), while an
815 elevated (altitude >1 km) dust aerosol layer (α_{532} ~1.0 km⁻¹) at the edge of the CALIPSO track
816 over the Taklamakan desert (above 38 °N). Over southern India (below 17 °N) polluted continental
817 aerosols prevail (α_{532} between 0.5-0.8 km⁻¹) and mostly accumulate within the boundary layer
818 (~1.5 km a.s.l.), while over northern India (above 19 °N), the aerosol situation includes a mixture
819 of polluted continental and polluted dust (α_{532} ~1.6 km⁻¹ below 1 km altitude). The corresponding
820 vertical cross-section of retrieved N_{CN} and N_{CCN} at a supersaturation of 0.4% using ECLiAP can
821 be seen in Figures 8c and 8d, respectively. N_{CN} and N_{CCN} larger than 25000 cm⁻³ and 3000 cm⁻³ at
822 a supersaturation of 0.4% appear over the areas where polluted continental aerosols dominate
823 (southern India), while N_{CCN} is greater than 2000 cm⁻³ appears over northern India. Dust N_{CCN} of
824 100 to 200 cm⁻³ appears over the Taklamakan desert region.

Deleted: Over southern India (below 17 °N),

825 To verify the capability of ECLiAP retrieval to capture similar variability of particle
826 physicochemical characteristics and its influence on CCN retrievals, we have investigated two
827 distinct cases identified based on the variation in aerosol subtypes and meteorological variables.
828 These scenarios are as follows: (1) Case-I: domination of polluted continental aerosols over
829 southern India (red color box covered in figure 8) (2) Case-II: Mixture of polluted dust and polluted
830 continental aerosols over northern India (blue color box covered in figure 8). The profiles of
831 extinction coefficients at 532 nm and relative humidity, along with retrieved N_{CN} and N_{CCN} at six
832 supersaturations, are presented in Figure 9. Figure 9a shows the profiles of the extinction
833 coefficient at 532 nm and relative humidity for both cases. The extinction profile in case-I ranges
834 from 0.7-1.2 km⁻¹, is dominated by polluted continental aerosols in the high moisture condition
835 (RH between 60%-80%), accumulates within the boundary layer (~1.5 km), and peaks at ~1.2 km.
836 Conversely, case-II represents the low moisture condition (RH ≤ 30%), with relatively large
837 extinction coefficient values with a maximum of 1.6 km⁻¹ at ~0.2 km altitude, influenced mainly
838 by the mixture of polluted continental and polluted dust aerosols. These two cases are dynamically
839 diverse and different in nature that providing a solid platform to verify the capability of ECLiAP
840 in retrieving N_{CCN} . Figure 9b illustrates the retrieved N_{CN} using ECLiAP for both cases. The
841 retrieved mean values of N_{CN} are observed to be almost similar (~12000 cm⁻³ and ~11000 cm⁻³ for
842 case-I and case-II, respectively). The profiles of N_{CN} follow a similar vertical distribution pattern
843 of extinction coefficients. Figures 9c and 9d display the retrieved N_{CCN} at six supersaturations for
844 Case-I and II, respectively. Interestingly, N_{CCN} values are found to be relatively lower in case-II,
845 though its extinction coefficient is larger than in case-I. Note that ECLiAP considers polluted dust
846 as a mixture of polluted continental and dust aerosol to retrieve N_{CCN} . The above-mentioned
847 discrepancy can be only explained by the intrusion of dust and its non-hygroscopic behavior along

Deleted: peaking

Deleted: the

851 with dry conditions, further reducing the concentration of hygroscopic aerosols that leads to a
852 decrease in N_{CCN} . This has been clearly reflected in the calculated activation ratio ($AR =$
853 N_{CCN}/N_{CN}) spectra in Figure S5. Figure S5 directly compares the AR spectra as a function of SS
854 for both cases. The observed differences in the AR spectra reflect the nature of the particles to act
855 as CCN. Relatively, larger values of AR in case-I indicate the dominance of hygroscopic aerosols
856 get activated to CCN under high moisture and increase N_{CCN} . In contrast, the dust intrusion in
857 case-II reduces the capability of particles to activate as CCN under low moisture and further
858 reduces AR by ~20%-60% for the range of supersaturation from 0.07% to 1.0%. Given the limited
859 sample space, the aim of the study is to demonstrate the potential of ECLiAP for retrieving reliable
860 N_{CCN} data from spaceborne lidar measurements. We have adapted the retrieval approach to
861 accommodate the available data, utilizing aerosol optical properties at two wavelengths and
862 meteorological datasets. These modifications introduce potential limitations and uncertainties due
863 to the availability of limited number of input parameters. While the CALIPSO case study offers
864 valuable insights, we stress the need for further validation with independent measurements. A
865 detailed comprehensive analysis comparing the CALIOP-retrieved N_{CCN} with multi-campaign
866 airborne measurements is essential to evaluate the reliability of ECLiAP to construct the 3D CCN
867 climatology at a global scale.

868 5 Discussion

869 Due to the absence of vertically resolved information in AOD, using it as a proxy for CCN in ACI
870 studies has several shortcomings. Among other issues, a column property like AOD is not
871 necessarily representative of N_{CCN} at altitudes, which affects the formation and growth of the cloud.
872 Because no reliable global estimate of N_{CCN} exists, the fundamental assumptions of ACI cannot
873 be robustly verified with the available sparse and localized in-situ measurements. In this study, we
874 present a novel approach based on the $3\beta+3\alpha$ technique for retrieving vertically-resolved cloud-
875 relevant N_{CCN} from a single spaceborne lidar sensor. With this development, we demonstrate a
876 new application of active satellite remote sensing that can provide direct measurements of CCN to
877 improve understanding of ACI processes.

878 To address the problem of the non-uniqueness of a solution in the $3\beta+2\alpha$ inverse technique, we
879 have adopted a more realistic LUT-based approach using the $3\beta+3\alpha$ multiwavelength technique,
880 reflecting the bimodal particle distribution in the atmosphere better. Previous studies (Ly et al.,
881 2018; Tan et al., 2019) demonstrated that CCN estimation is highly sensitive to the extinction
882 coefficient than the backscatter coefficient. Therefore, leveraging the availability of derived
883 extinction coefficients at 1064 nm as an additional input to ECLiAP to improve the retrieval
884 accuracy of particle size distribution, particularly for coarse mode. In order to verify the
885 performance, the CCN estimation error, using Eq. 12, has been calculated using both $3\beta+2\alpha$ and
886 $3\beta+3\alpha$ techniques for each aerosol subtype in comparison to the observed CCN values. The
887 relative difference in CCN estimation error between $3\beta+2\alpha$ and $3\beta+3\alpha$ techniques for each aerosol
888 subtype is shown in Figure 10. The analysis shows that insertion of the α_{1064} signal in the $3\beta+3\alpha$
889 technique improves the CCN estimation by ~15% in total and ~20% for the coarse mode dominated

Deleted: new

Deleted: Lv et al., 2018; Tan et al., 2019

Deleted: we have included an additional signal of extinction coefficient at 1064 nm

894 aerosol subtypes (i.e., marine and dust aerosols) compared to $3\beta+2\alpha$. Based on CCN closure
895 analysis, Patel & Jiang, (2021), suggested that particle size and chemical composition are more
896 crucial in the CCN activity at lower SS. In contrast, at higher SS, most particles become activated
897 regardless of their size and composition. Therefore, the improvement in CCN estimation is
898 relatively large in low SS ($SS < 0.2\%$) than in high SS ($SS > 0.2\%$). In our N_{CCN} retrieval approach,
899 we use multiple input parameters: aerosol optical properties (α_{355} , α_{532} , α_{1064} , β_{355} , β_{532} , and β_{1064})
900 and relative humidity (RH). Each parameter plays a unique role in constraining aerosol size and
901 concentration accurately. Through sensitivity analyses, we found that using all seven parameters
902 leads to improved retrieval accuracy compared to a reduced set. The interplay between the
903 parameters enhances the performance of algorithm, resulting in reliable and consistent N_{CCN}
904 retrievals. The combination of aerosol optical properties and RH provides a comprehensive
905 understanding of aerosol behavior, ensuring a more holistic characterization of aerosol properties
906 in our study.

Deleted: Patel & Jiang, (2021)

Formatted: Subscript

Formatted: Subscript

Formatted: Subscript

Formatted: Subscript

Formatted: Subscript

Formatted: Subscript

Formatted: Subscript

Formatted: Subscript

907 Systematic and random errors in the lidar measurements were evaluated individually and discussed
908 in the sensitivity analysis. Both systematic and random errors realistically coexist in optical
909 parameters, and therefore, we have evaluated their concurrent effect. The simulations were
910 conducted with both systematic and random errors co-occurring. The results (not shown here)
911 show that the retrieved CCN errors are much smaller than the error obtained individually by either
912 systematic or random at each wavelength independently. The mean CCN error ranges between
913 7%-15% at SS from 0.07% to 1.0%. This retrieved CCN error is slightly large (~12%-18%) for
914 the coarse-mode dominated aerosol subtypes (dust and marine). Summing up errors from multiple
915 optical parameters might compensate for each other and improve the CCN retrievals. Furthermore,
916 the retrieval from ECLiAP has few constraints. (i) it strongly depends on the accuracy of lidar-
917 measured aerosol optical properties. The retrieval is only possible if the lidar signals are available
918 at least at two wavelengths. (ii) the non-spherical shape of dust particles. While this study considers
919 the spheroidal shape of dust particles, a recent study by Haerig et al., (2022), suggested that the
920 assumption of spheroidal dust particle have limitations in obtaining an accurate particle
921 depolarization ratio. Therefore, our assumption of spheroidal shape may not fully capture the
922 complexity of dust particles and could lead to uncertainties in our dust-related retrieval. Although
923 complex non-spherical shape models (Gasteiger et al., 2011; Saito et al., 2021), provide a more
924 realistic representation of irregularly shaped dust particles, they are computationally expensive.
925 We acknowledge this limitation and plan to explore alternative models in future studies. (iii)
926 retrieval from ECLiAP is only performed for $RH \leq 99\%$. (iv) The use of mean refractive indices
927 for each aerosol subtype in the creation of the look-up tables may limit the representation of
928 refractive index variability within each subtype. This simplified approach reduces computation
929 time but may compromise the accuracy of the LUTs in accounting for the full range of aerosol
930 properties. (v) The CCN activity also depends on the mixing state, which is difficult to measure
931 from space. Subsequently, an alternative solution is required to parametrize the effect of the mixing
932 state on CCN activity. (vi) It is constrained by the inherent limitations of lidar measurements, which
933 may not effectively capture particles with sizes smaller than 50 nanometers. Consequently, the

Deleted:

Deleted: Haerig et al., (2022)

Deleted: (Gasteiger et al., 2011; Saito et al., 2021)

Deleted: i

Deleted: ii

Deleted: the

Deleted: the

942 algorithm does not fully account for the impact of new particle formation on the estimation of
943 CCN concentrations.

Deleted:

944 The present study demonstrates the capability of ECLiAP to construct the three-dimensional global
945 climatology of N_{CCN} . The global coverage of N_{CCN} , in conjunction with collocated retrieved cloud
946 properties, will provide crucial input for the regional and global simulations that will provide
947 realistic assessments of aerosol-induced cloud radiative forcing. The satellite-retrieved N_{CCN} can
948 precisely separate the aerosols into natural and anthropogenic components, which can be further
949 used for constraining aerosol emissions and transport models for air-quality studies. The
950 application of detailed N_{CCN} will potentially mitigate the uncertainty of aerosol perturbed climate
951 forcing (direct + indirect) and improve confidence in assessing anthropogenic contributions and
952 climate change projections.

Deleted: the

953 6 Summary

954 CCN number concentration is a critically-important parameter to constrain the relationship
955 between aerosols and clouds and is needed to improve the understanding of ACI processes. The
956 lack of direct measurements of CCN prevents robust testing of the underlying assumptions
957 associated with aerosol-cloud interactions robustly and evaluates climate model simulations. In
958 order to overcome this limitation, we presented ECLiAP, an emergent remote sensing-based
959 analytical algorithm based on the physical law to retrieve the vertically resolved N_{CCN} from aerosol
960 optical properties measured by the multiwavelength lidar system. Among the several fundamental
961 aspects of the mathematical problem that must be solved during retrievals of microphysical
962 parameters from multiwavelength lidar, the most crucial aspect is that the inverse solution is not
963 unique. Therefore, the retrieval is implemented based on look-up tables generated from Mie
964 scattering (and T-matrix/IGOM for dust particles) calculations. AERONET-based five
965 representative aerosol subtypes with bimodal size distributions were considered. The influence of
966 relative humidity on lidar-measured aerosol optical properties is corrected using the aerosol type-
967 dependent hygroscopic growth factor to obtain the dry aerosol optical properties. As a tradeoff
968 between the accuracy and computation time of the inversion, a successive approximation technique
969 is utilized in two steps to retrieve the optically equivalent particle number size distribution. Once
970 the aerosol size distribution parameters are obtained through the LUT, critical diameter and N_{CCN}
971 at six supersaturations ranging from 0.07% to 1.0% is estimated using the κ -Köhler theory.

Deleted: evaluate

972 Sensitivity analyses were carried out to evaluate the algorithm performance and to show the
973 influence of systematic and random errors of lidar-derived optical properties and auxiliary RH
974 profiles on CCN retrieval. The performance of ECLiAP is evaluated with error-free data, and N_{CCN}
975 at all six supersaturations is well reproduced with good accuracy and stability for the five aerosol
976 subtypes. Systematic errors in extinction coefficients and RH greatly influence CCN retrieval
977 errors. Reducing uncertainties in extinction coefficients effectively improves retrieval accuracy,
978 while uncertainties in backscatter coefficients benefit retrieval at higher SS. Differences in weights
979 of fine- to coarse-mode particles within the aerosol subtypes lead to significant differences in the

Deleted: the

Deleted: coarse mode

985 retrieval uncertainty. The differences can be explained via the weaker **constraint** of the algorithm
986 for the coarse mode particles than for the fine mode. However, **the** insertion of the additional signal
987 at a relatively longer wavelength reduced the differences in the retrieval uncertainty compared to
988 previous techniques. The mean random errors are relatively small and found **to be** relatively large
989 for the coarse mode-dominated aerosol subtypes, consistent with the sensitivities to the systematic
990 errors. In realistic cases, systematic and random errors often offset each other and improve the
991 mean CCN retrievals. Overall, the error analysis suggests that extinction coefficients at 355 and
992 532 nm must be reliably derived to ensure retrieval accuracy, including measurements at longer
993 wavelengths further improve the CCN retrievals, particularly for the coarse mode-dominated
994 aerosol subtypes.

Deleted: constrain

995 The ECLiAP algorithm was applied to observational data from the NASA ORACLES airborne
996 campaign to illustrate the potential of the algorithm. N_{CCN} retrieved from lidar (HSRL-2)
997 measurements have been validated against the simultaneous measurements from the CCN counter
998 installed in the flight. Considering the inhomogeneity in the vertical distribution of aerosols
999 throughout the atmospheric column, N_{CCN} from in situ measurements and lidar retrievals agree
1000 well. Furthermore, for the first time, the ECLiAP has been applied to spaceborne lidar
1001 measurements – CALIOP/CALIPSO – to retrieve N_{CCN} . The results demonstrate that the N_{CCN}
1002 retrieved by ECLiAP is highly influenced by the variability of aerosol particle size and
1003 composition based on aerosol subtypes and also captures the meteorological influence. The
1004 **vertically resolved** information of aerosols, along with CCN from spaceborne lidar, is essential for
1005 investigating the ACI in detail.

Deleted: vertically-resolved

1006 Our future goals include a comprehensive evaluation of N_{CCN} derived from spaceborne lidar
1007 measurements, i.e., CALIOP/CALIPSO, with multi-campaign airborne measurements, covering
1008 various physicochemical regimes in the troposphere. The extensive validation will enable us to
1009 test the applicability of the ECLiAP algorithm in the context of estimating the N_{CCN} from space.
1010 Eventually, we plan to apply the ECLiAP algorithm over the period of CALIOP observations (~15
1011 years) to generate the global three-dimensional N_{CCN} climatology. The data set coupled with the
1012 cloud-related data from the other satellite or state-of-the-art numerical models will help improve
1013 our understanding of the ACI. The science narrative of **the** NASA Aerosol and Cloud, Convection
1014 and Precipitation (ACCP) project pointed out that the combination of **near-simultaneous** and
1015 collocated lidar and polarimeter measurements can provide more detailed information regarding
1016 particle size, concentration, and composition (Braun et al., 2022). Therefore, our future work may
1017 also include combining the lidar measurements with passive observations in the ECLiAP algorithm
1018 to further narrow down the uncertainty of aerosol microphysics with the enhanced observational
1019 constraints (Xu et al., 2021), which will in turn improve the accuracy of CCN retrieval. Moreover,
1020 the ability of CALIOP to detect the aerosol subtypes has facilitated the retrieval of aerosol type-
1021 specific 3D N_{CCN} climatology on a global scale. These datasets from spaceborne lidar
1022 measurements will be beneficial for evaluating models and other satellite products, opening a new
1023 window to investigate the region and regime-wise detailed ACI studies and better constraining
1024 anthropogenic contributions to the climate forcing in the climate model.

Deleted: near simultaneous

Deleted: (Braun et al., 2022)

Deleted: (Xu et al., 2021)

Deleted: Page Break

Deleted: ¶
Appendix A1: Separation of optical properties for dust mixture¶

We have adopted the methodology by Tesche et al., (2009) to separate the dust and non-dust extinction coefficients in the dust mixtures (polluted dust and dusty marine) using particle backscatter coefficients and particle depolarization ratio. The optical properties ¶

$$\beta_a = \beta_p \frac{(\delta_p - \delta_2)(1 + \delta_1)}{(\delta_1 - \delta_2)(1 + \delta_p)}$$

... [1]

1041
1042 **Data availability statement.** All data that support the findings of this study are publicly available.
1043 The in-situ measurements at the ARM-SGP are available at
1044 <https://www.arm.gov/capabilities/observatories/sgp>.
1045 All ORACLES data are accessible via the digital object identifiers (DOIs) provided under
1046 ORACLES science team.
1047 references: https://doi.org/10.5067/Suborbital/ORACLES/P3/2018_V2 (ORACLES Science
1048 Team, 2020a), https://doi.org/10.5067/Suborbital/ORACLES/P3/2017_V2 (ORACLES Science
1049 Team, 2020b).
1050 The CALIPSO data are available at <https://eosweb.larc.nasa.gov/>.

1051
1052 **Author contributions.** PNP conceptualized and designed the study. PNP carried out the data
1053 analysis and interpretation with contributions from JHJ, RG and HG. PNP wrote the manuscript.
1054 JHJ, RG, HG, OVK, MJG, LG, FX and OA reviewed, commented and/or edited the manuscript.

1055 **Competing Interests:** The contact author has declared that none of the authors has any competing
1056 interests.

1057 **Acknowledgment.** This work was conducted at the NASA-sponsored Jet Propulsion Laboratory
1058 (JPL), California Institute of Technology, under contract by NASA. We appreciate the facility
1059 provided by the JPL for data analysis and research. This work was supported by the NASA
1060 Postdoctoral Program, administered by Oak Ridge Associated Universities under contract with
1061 NASA. We are thankful to Charles A. Brock (Chemical Sciences Laboratory, National Oceanic and
1062 Atmospheric Administration, Boulder, CO, USA) for the fruitful discussion on the present study. All
1063 data were obtained from the Atmospheric Radiation Measurement (ARM) Program sponsored by
1064 the U.S. Department of Energy, Office of Science, Office of Biological and Environmental
1065 Research, Climate and Environmental Sciences Division, and National Science Foundation. We
1066 thank the ORACLES deployment support teams and the science team for a successful and
1067 productive mission. We thank the CALIPSO science team, for providing the CALIPSO data.

1068

1069 References

1070 [Andreae, M. O., & Rosenfeld, D. \(2008\). Aerosol-cloud-precipitation interactions. Part I. The nature and](#)
1071 [sources of cloud-active aerosols. *Earth-Science Reviews*, 89\(1–2\), 13–41.](#)
1072 <https://doi.org/10.1016/j.earscirev.2008.03.001>

1073 [Bedoya-Velásquez, A. E., Navas-Guzmán, F., Granados-Muñoz, M. J., Titos, G., Román, R., Andrés](#)
1074 [Casquero-Vera, J., Ortiz-Amezcu, P., Antonio Benavent-Oltra, J., de Arruda Moreira, G., Montilla-](#)
1075 [Rosero, E., Hoyos, C. D., Artiñano, B., Coz, E., Olmo-Reyes, F. J., Alados-Arboledas, L., & Guerrero-](#)
1076 [Rascado, J. L. \(2018\). Hygroscopic growth study in the framework of EARLINET during the SLOPE](#)
1077 [i campaign: Synergy of remote sensing and in situ instrumentation. *Atmospheric Chemistry and*](#)
1078 [Physics, 18\(10\), 7001–7017. https://doi.org/10.5194/ACP-18-7001-2018](#)

Formatted: Font: 11 pt

Formatted: Justified

1079 [Bi, L., Yang, P., Kattawar, G. W., & Kahn, R. \(2009\). Single-scattering properties of triaxial ellipsoidal](#)
1080 [particles for a size parameter range from the Rayleigh to geometric-optics regimes. *Applied Optics*,](#)
1081 [48\(1\), 114–126. <https://doi.org/10.1364/AO.48.000114>](#)

1082 [Bohren, C. F., & Huffman, D. R. \(1998\). Absorption and Scattering of Light by Small Particles. *Absorption*](#)
1083 [and *Scattering of Light by Small Particles*. <https://doi.org/10.1002/9783527618156>](#)

1084 [Bony, S., & Dufresne, J. L. \(2005\). Marine boundary layer clouds at the heart of tropical cloud feedback](#)
1085 [uncertainties in climate models. *Geophysical Research Letters*, 32\(20\), 1–4.](#)
1086 [<https://doi.org/10.1029/2005GL023851>](#)

1087 [Braun, S., Stephens, G., Berndt, E., Blanchard, Y., Blanchet, J.-P., Carmichael, G., da Silva, A., Ferrare,](#)
1088 [R., Ivanco, M., Kacenelenbogen, M., Kirschbaum, D., Libois, Q., Mace, G., Omar, A., Petersen, W.,](#)
1089 [Redemann, J., Seidel, F., van den Heever, S., Waliser, D., & Winker, D. \(2022\). *Aerosol, Cloud,*](#)
1090 [*Convection, and Precipitation \(ACCP\) Science & Applications*.](#)
1091 [\[https://aos.gsfc.nasa.gov/docs/ACCP_Science_Narrative-\\(Mar2022\\).pdf\]\(https://aos.gsfc.nasa.gov/docs/ACCP_Science_Narrative-\(Mar2022\).pdf\)](#)

1092 [Brock, C. A., Wagner, N. L., Anderson, B. E., Attwood, A. R., Beyersdorf, A., Campuzano-Jost, P., Carlton,](#)
1093 [A. G., Day, D. A., Diskin, G. S., Gordon, T. D., Jimenez, J. L., Lack, D. A., Liao, J., Markovic, M.](#)
1094 [Z., Middlebrook, A. M., Ng, N. L., Perring, A. E., Richardson, M. S., Schwarz, J. P., ... Murphy, D.](#)
1095 [M. \(2016\). Aerosol optical properties in the southeastern United States in summer - Part 1:](#)
1096 [Hygroscopic growth. *Atmospheric Chemistry and Physics*, 16\(8\), 4987–5007.](#)
1097 [<https://doi.org/10.5194/ACP-16-4987-2016>](#)

1098 [Burkart, J., Steiner, G., Reischl, G., & Hitznerberger, R. \(2011\). Long-term study of cloud condensation](#)
1099 [nuclei \(CCN\) activation of the atmospheric aerosol in Vienna. *Atmospheric Environment*, 45\(32\),](#)
1100 [5751–5759. <https://doi.org/10.1016/J.ATMOSENV.2011.07.022>](#)

1101 [Burton, S. P., Chemyakin, E., Liu, X., Knobelspiesse, K., Starnes, S., Sawamura, P., Moore, R. H.,](#)
1102 [Hostetler, C. A., & Ferrare, R. A. \(2016\). Information content and sensitivity of the 3β + 2α lidar](#)
1103 [measurement system for aerosol microphysical retrievals. *Atmospheric Measurement Techniques*,](#)
1104 [9\(11\), 5555–5574. <https://doi.org/10.5194/AMT-9-5555-2016>](#)

1105 [Burton, S. P., Ferrare, R. A., Hostetler, C. A., Hair, J. W., Rogers, R. R., Obland, M. D., Butler, C. F., Cook,](#)
1106 [A. L., Harper, D. B., & Froyd, K. D. \(2012\). Aerosol classification using airborne High Spectral](#)
1107 [Resolution Lidar measurements—methodology and examples. *Atmospheric Measurement Techniques*,](#)
1108 [5\(1\), 73–98. <https://doi.org/10.5194/AMT-5-73-2012>](#)

1109 [Burton, S. P., Hostetler, C. A., Cook, A. L., Hair, J. W., Seaman, S. T., Scola, S., Harper, D. B., Smith, J.](#)
1110 [A., Fenn, M. A., Ferrare, R. A., Saide, P. E., Chemyakin, E. V., & Müller, D. \(2018\). Calibration of](#)
1111 [a high spectral resolution lidar using a Michelson interferometer, with data examples from](#)
1112 [ORACLES. *Applied Optics*, 57\(21\), 6061. <https://doi.org/10.1364/AO.57.006061>](#)

1113 [Carslaw, K. S., Boucher, O., Spracklen, D. v., Mann, G. W., L. Rae, J. G., Woodward, S., & Kulmala, M.](#)
1114 [\(2010\). A review of natural aerosol interactions and feedbacks within the Earth system. *Atmospheric*](#)
1115 [*Chemistry and Physics*, 10\(4\), 1701–1737. <https://doi.org/10.5194/ACP-10-1701-2010>](#)

1116 [Chang, I., Gao, L., Burton, S. P., Chen, H., Diamond, M. S., Ferrare, R. A., Flynn, C. J., Kacenelenbogen,](#)
1117 [M., LeBlanc, S. E., Meyer, K. G., Pistone, K., Schmidt, S., Segal-Rozenhaimer, M., Shinozuka, Y.,](#)
1118 [Wood, R., Zuidema, P., Redemann, J., & Christopher, S. A. \(2021\). Spatiotemporal Heterogeneity of](#)

1119 [Aerosol and Cloud Properties Over the Southeast Atlantic: An Observational Analysis. *Geophysical*](#)
1120 [Research Letters, 48\(7\). <https://doi.org/10.1029/2020GL091469>](#)

1121 [Chemyakin, E., Burton, S., Kolgotin, A., Müller, D., Hostetler, C., & Ferrare, R. \(2016\). Retrieval of aerosol](#)
1122 [parameters from multiwavelength lidar: investigation of the underlying inverse mathematical](#)
1123 [problem. *Applied Optics*, 55\(9\), 2188. <https://doi.org/10.1364/AO.55.002188>](#)

1124 [Choudhury, G., & Tesche, M. \(2022\). Estimating cloud condensation nuclei concentrations from CALIPSO](#)
1125 [lidar measurements. *Atmospheric Measurement Techniques*, 15\(3\), 639–654.](#)
1126 [<https://doi.org/10.5194/AMT-15-639-2022>](#)

1127 [Clarke, A., & Kapustin, V. \(2010\). Hemispheric aerosol vertical profiles: Anthropogenic impacts on optical](#)
1128 [depth and cloud nuclei. *Science*, 329\(5998\), 1488–1492.](#)
1129 [\[https://doi.org/10.1126/SCIENCE.1188838/SUPPL_FILE/CLARKE.SOM.PDF\]\(https://doi.org/10.1126/SCIENCE.1188838/SUPPL_FILE/CLARKE.SOM.PDF\)](#)

1130 [Coddington, O. M., Pilewskie, P., Redemann, J., Platnick, S., Russell, P. B., Schmidt, K. S., Gore, W. J.,](#)
1131 [Livingston, J., Wind, G., & Vukicevic, T. \(2010\). Examining the impact of overlying aerosols on the](#)
1132 [retrieval of cloud optical properties from passive remote sensing. *Journal of Geophysical Research*](#)
1133 [Atmospheres, 115\(10\). <https://doi.org/10.1029/2009JD012829>](#)

1134 [Dubovik, O. \(2002\). Variability of absorption and optical properties of key aerosol types observed in](#)
1135 [worldwide locations. *J. Atmos. Sci.*, 59, 590–608. \[https://doi.org/10.1175/1520-\]\(https://doi.org/10.1175/1520-0469\(2002\)059<0590:voaaop>2.0.co\)](#)
1136 [0469\(2002\)059<0590:voaaop>2.0.co](#)

1137 [Dubovik, O., Sinyuk, A., Lapyonok, T., Holben, B. N., Mishchenko, M., Yang, P., Eck, T. F., Volten, H.,](#)
1138 [Muñoz, O., Veihelmann, B., van der Zande, W. J., Leon, J. F., Sorokin, M., & Slutsker, I. \(2006\).](#)
1139 [Application of spheroid models to account for aerosol particle nonsphericity in remote sensing of](#)
1140 [desert dust. *Journal of Geophysical Research Atmospheres*, 111\(11\).](#)
1141 [<https://doi.org/10.1029/2005JD006619>](#)

1142 [Dusek, U., Frank, G. P., Hildebrandt, L., Curtius, J., Schneider, J., Walter, S., Chand, D., Drewnick, F.,](#)
1143 [Hings, S., Jung, D., Borrmann, S., & Andreae, M. O. \(2006\). Size matters more than chemistry for](#)
1144 [cloud-nucleating ability of aerosol particles. *Science*. <https://doi.org/10.1126/science.1125261>](#)

1145 [Fan, J., Wang, Y., Rosenfeld, D., & Liu, X. \(2016\). Review of Aerosol–Cloud Interactions: Mechanisms,](#)
1146 [Significance, and Challenges. *Journal of the Atmospheric Sciences*, 73\(11\), 4221–4252.](#)
1147 [<https://doi.org/10.1175/JAS-D-16-0037.1>](#)

1148 [Feingold, G., Yang, S., Hardesty, R. M., & Cotton, W. R. \(1998\). Feasibility of retrieving cloud](#)
1149 [condensation nucleus properties from doppler cloud radar, microwave radiometer, and lidar. *Journal*](#)
1150 [of Atmospheric and Oceanic Technology](#). [https://doi.org/10.1175/1520-](https://doi.org/10.1175/1520-0426(1998)015<1188:FORCCN>2.0.CO;2)
1151 [0426\(1998\)015<1188:FORCCN>2.0.CO;2](#)

1152 [Fernández, A. J., Molero, F., Becerril-Valle, M., Coz, E., Salvador, P., Artiñano, B., & Pujadas, M. \(2018\).](#)
1153 [Application of remote sensing techniques to study aerosol water vapour uptake in a real atmosphere.](#)
1154 [*Atmospheric Research*, 202, 112–127. <https://doi.org/10.1016/J.ATMOSRES.2017.11.020>](#)

1155 [Gasteiger, J., Wiegner, M., Groß, S., Freudenthaler, V., Toledano, C., Tesche, M., & Kandler, K. \(2011\).](#)
1156 [Modelling lidar-relevant optical properties of complex mineral dust aerosols. *Tellus, Series B:*](#)
1157 [*Chemical and Physical Meteorology*, 63\(4\), 725–741. \[https://doi.org/10.1111/J.1600-\]\(https://doi.org/10.1111/J.1600-0889.2011.00559.X\)](#)
1158 [0889.2011.00559.X](#)

1159 [Ghan, S. J., & Collins, D. R. \(2004\). Use of in situ data to test a Raman lidar-based cloud condensation](#)
1160 [nuclei remote sensing method. *Journal of Atmospheric and Oceanic Technology*.](#)
1161 [https://doi.org/10.1175/1520-0426\(2004\)021<0387:UOISDT>2.0.CO;2](https://doi.org/10.1175/1520-0426(2004)021<0387:UOISDT>2.0.CO;2)

1162 [Ghan, S. J., Rissman, T. A., Elleman, R., Ferrare, R. A., Turner, D., Flynn, C., Wang, J., Orgen, J., Hudson,](#)
1163 [J., Jonsson, H. H., VanReken, T., Flagan, R. C., & Seinfeld, J. H. \(2006\). Use of situ cloud](#)
1164 [condensation nuclei, extinction, and aerosol size distribution measurements to test a method for](#)
1165 [retrieving cloud condensation nuclei profiles from surface measurements. *Journal of Geophysical*](#)
1166 [Research Atmospheres, 111\(5\).](#) <https://doi.org/10.1029/2004JD005752>

1167 [Giannakaki, E., Van Zyl, P. G., Müller, D., Balis, D., & Komppula, M. \(2016\). Optical and microphysical](#)
1168 [characterization of aerosol layers over South Africa by means of multi-wavelength depolarization and](#)
1169 [Raman lidar measurements. *Atmospheric Chemistry and Physics*, 16\(13\), 8109–8123.](#)
1170 <https://doi.org/10.5194/ACP-16-8109-2016>

1171 [Gryspeerd, E., & Stier, P. \(2012\). Regime-based analysis of aerosol-cloud interactions. *Geophysical*](#)
1172 [Research Letters.](#) <https://doi.org/10.1029/2012GL053221>

1173 [Haarig, M., Ansmann, A., Engelmann, R., Baars, H., Toledano, C., Torres, B., Althausen, D., Radenz, M.,](#)
1174 [& Wandinger, U. \(2022\). First triple-wavelength lidar observations of depolarization and extinction-](#)
1175 [to-backscatter ratios of Saharan dust. *Atmospheric Chemistry and Physics*, 22\(1\), 355–369.](#)
1176 <https://doi.org/10.5194/ACP-22-355-2022>

1177 [Hänel, A., Baars, H., Althausen, D., Ansmann, A., Engelmann, R., & Sun, J. Y. \(2012\). One-year aerosol](#)
1178 [profiling with EUCAARI Raman lidar at Shangdianzi GAW station: Beijing plume and seasonal](#)
1179 [variations. *Journal of Geophysical Research Atmospheres*, 117\(13\).](#)
1180 <https://doi.org/10.1029/2012JD017577>

1181 [Hatch, T., & Choate, S. P. \(1929\). Statistical description of the size properties of non uniform particulate](#)
1182 [substances. *Journal of the Franklin Institute*, 207\(3\), 369–387.](#) <https://doi.org/10.1016/S0016->
1183 [0032\(29\)91451-4](0032(29)91451-4)

1184 [IPCC. \(2013\). Working Group I Contribution to the IPCC Fifth Assessment Report, Climate Change 2013:](#)
1185 [The Physical Science Basis. *Ippc, AR5*\(March 2013\), 2014.](#)
1186 <https://doi.org/10.1017/CBO9781107415324.Summary>

1187 [IPCC. \(2014\). Climate Change 2014: Synthesis Report. Contribution of Working Groups I, II and III to the](#)
1188 [Fifth Assessment Report of the Intergovernmental Panel on Climate Change. In *Core Writing Team,*](#)
1189 [R.K. Pachauri and L.A. Meyer. IPCC.](#) <https://doi.org/10.1017/CBO9781107415324.004>

1190 [Jurányi, Z., Gysel, M., Weingartner, E., Decarlo, P. F., Kammernann, L., & Baltensperger, U. \(2010\).](#)
1191 [Measured and modelled cloud condensation nuclei number concentration at the high alpine site](#)
1192 [Jungfraujoch. *Atmospheric Chemistry and Physics*, 10\(16\), 7891–7906.](#) <https://doi.org/10.5194/ACP->
1193 <10-7891-2010>

1194 [Kacarab, M., Lee Thornhill, K., Dobracki, A., Howell, S. G., O'Brien, J. R., Freitag, S., Poellot, M. R.,](#)
1195 [Wood, R., Zuidema, P., Redemann, J., & Nenes, A. \(2020\). Biomass burning aerosol as a modulator](#)
1196 [of the droplet number in the southeast Atlantic region. *Atmospheric Chemistry and Physics*, 20\(5\),](#)
1197 <3029–3040. https://doi.org/10.5194/ACP-20-3029-2020>

1198 [Kantorovitch, L. \(1939\). The method of successive approximation for functional equations. *Acta*](#)
1199 [Mathematica, 71\(1\), 63–97.](#) <https://doi.org/10.1007/BF02547750>

1200 [Kapustin, V. N., Clarke, A. D., Shinozuka, Y., Howell, S., Brekhovskikh, V., Nakajima, T., & Higurashi,](#)
1201 [A. \(2006\). On the determination of a cloud condensation nuclei from satellite: Challenges and](#)
1202 [possibilities. *Journal of Geophysical Research Atmospheres*. <https://doi.org/10.1029/2004JD005527>](#)

1203 [Kasten, F. \(1969\). Visibility forecast in the phase of pre-condensation. *Tellus*, *21*\(5\), 631–635.](#)
1204 [https://doi.org/10.3402/TELLUSA.V21I5.10112](#)

1205 [Kim, M. H., Omar, A. H., Tackett, J. L., Vaughan, M. A., Winker, D. M., Trepte, C. R., Hu, Y., Liu, Z.,](#)
1206 [Poole, L. R., Pitts, M. C., Kar, J., & Magill, B. E. \(2018\). The CALIPSO version 4 automated aerosol](#)
1207 [classification and lidar ratio selection algorithm. *Atmospheric Measurement Techniques*, *11*\(11\),](#)
1208 [6107–6135. <https://doi.org/10.5194/AMT-11-6107-2018>](#)

1209 [Koehler, K. A., Kreidenweis, S. M., DeMott, P. J., Petters, M. D., Prenni, A. J., & Carrico, C. M. \(2009\).](#)
1210 [Hygroscopicity and cloud droplet activation of mineral dust aerosol. *Geophysical Research Letters*,](#)
1211 [36\(8\). <https://doi.org/10.1029/2009GL037348>](#)

1212 [Kolmogorov, A. N. \(1941\). About the Logarithmic-normal Law of Particle Size Distribution during](#)
1213 [Crushing. *Proceedings of the USSR Academy of Sciences*, *31*\(2\), 99–101.](#)

1214 [Kompula, M., Mielonen, T., Arola, A., Korhonen, K., Lihavainen, H., Hyvärinen, A. P., Baars, H.,](#)
1215 [Engelmann, R., Althausen, D., Ansmann, A., Müller, D., Panwar, T. S., Hooda, R. K., Sharma, V. P.,](#)
1216 [Kerminen, V. M., Lehtinen, K. E. J., & Viisanen, Y. \(2012\). Technical Note: One year of Raman-](#)
1217 [lidar measurements in Gual Pahari EUCAARI site close to New Delhi in India-Seasonal](#)
1218 [characteristics of the aerosol vertical structure. *Atmospheric Chemistry and Physics*, *12*\(10\), 4513–](#)
1219 [4524. <https://doi.org/10.5194/ACP-12-4513-2012>](#)

1220 [Kuang, Y., Zhao, C., Tao, J., Bian, Y., Ma, N., & Zhao, G. \(2017\). A novel method for deriving the aerosol](#)
1221 [hygroscopicity parameter based only on measurements from a humidified nephelometer system.](#)
1222 [*Atmospheric Chemistry and Physics*, *17*\(11\), 6651–6662. <https://doi.org/10.5194/ACP-17-6651-2017>](#)

1223 [Li, J., Liu, X., Yuan, L., Yin, Y., Li, Z., Li, P., Ren, G., Jin, L., Li, R., Dong, Z., Li, Y., & Yang, J. \(2015\).](#)
1224 [Vertical distribution of aerosol optical properties based on aircraft measurements over the Loess](#)
1225 [Plateau in China. *Journal of Environmental Sciences \(China\)*, *34*, 44–56.](#)
1226 [<https://doi.org/10.1016/J.JES.2015.01.021>](#)

1227 [Li, J., Yin, Y., Li, P., Li, Z., Li, R., Cribb, M., Dong, Z., Zhang, F., Li, J., Ren, G., Jin, L., & Li, Y. \(2015\).](#)
1228 [Aircraft measurements of the vertical distribution and activation property of aerosol particles over the](#)
1229 [Loess Plateau in China. *Atmospheric Research*, *155*, 73–86.](#)
1230 [<https://doi.org/10.1016/J.ATMOSRES.2014.12.004>](#)

1231 [Liu, J., & Li, Z. \(2014\). Estimation of cloud condensation nuclei concentration from aerosol optical](#)
1232 [quantities: Influential factors and uncertainties. *Atmospheric Chemistry and Physics*, *14*\(1\), 471–483.](#)
1233 [<https://doi.org/10.5194/ACP-14-471-2014>](#)

1234 [Liu, P. F., Zhao, C. S., Göbel, T., Hallbauer, E., Nowak, A., Ran, L., Xu, W. Y., Deng, Z. Z., Ma, N.,](#)
1235 [Mildenberger, K., Henning, S., Stratmann, F., & Wiedensohler, A. \(2011\). Hygroscopic properties of](#)
1236 [aerosol particles at high relative humidity and their diurnal variations in the north China plain.](#)
1237 [*Atmospheric Chemistry and Physics*, *11*\(7\), 3479–3494. <https://doi.org/10.5194/ACP-11-3479-2011>](#)

1238 [Liu, Z., Vaughan, M., Winker, D., Kittaka, C., Getzewich, B., Kuehn, R., Omar, A., Powell, K., Trepte, C.,](#)
1239 [& Hostetler, C. \(2009\). The CALIPSO lidar cloud and aerosol discrimination: Version 2 algorithm](#)

1240 and initial assessment of performance. *Journal of Atmospheric and Oceanic Technology*, 26(7), 1198–
1241 1213. <https://doi.org/10.1175/2009JTECHA1229.1>

1242 Lv, M., Liu, D., Li, Z., Mao, J., Sun, Y., Wang, Z., Wang, Y., & Xie, C. (2017). Hygroscopic growth of
1243 atmospheric aerosol particles based on lidar, radiosonde, and in situ measurements: Case studies from
1244 the Xinzhou field campaign. *Journal of Quantitative Spectroscopy and Radiative Transfer*, 188, 60–
1245 70. <https://doi.org/10.1016/J.JQSRT.2015.12.029>

1246 Lv, M., Wang, Z., Li, Z., Luo, T., Ferrare, R., Liu, D., Wu, D., Mao, J., Wan, B., Zhang, F., & Wang, Y.
1247 (2018). Retrieval of Cloud Condensation Nuclei Number Concentration Profiles From Lidar
1248 Extinction and Backscatter Data. *Journal of Geophysical Research: Atmospheres*, 123(11), 6082–
1249 6098. <https://doi.org/10.1029/2017JD028102>

1250 Mamouri, R. E., & Ansmann, A. (2016). Potential of polarization lidar to provide profiles of CCN-and INP-
1251 relevant aerosol parameters. *Atmospheric Chemistry and Physics*, 16(9), 5905–5931.
1252 <https://doi.org/10.5194/acp-16-5905-2016>

1253 Mattis, I., D'Amico, G., Baars, H., Amodeo, A., Madonna, F., & Iarlori, M. (2016). EARLINET Single
1254 Calculus Chain - Technical - Part 2: Calculation of optical products. *Atmospheric Measurement
1255 Techniques*, 9(7), 3009–3029. <https://doi.org/10.5194/AMT-9-3009-2016>

1256 Mishchenko, M. I., & Travis, L. D. (1998). Capabilities and limitations of a current FORTRAN
1257 implementation of the T-matrix method for randomly oriented, rotationally symmetric scatterers.
1258 *Journal of Quantitative Spectroscopy and Radiative Transfer*, 60(3), 309–324.
1259 [https://doi.org/10.1016/S0022-4073\(98\)00008-9](https://doi.org/10.1016/S0022-4073(98)00008-9)

1260 Molod, A., Takacs, L., Suarez, M., & Bacmeister, J. (2015). Development of the GEOS-5 atmospheric
1261 general circulation model: Evolution from MERRA to MERRA2. *Geoscientific Model Development*,
1262 8(5), 1339–1356. <https://doi.org/10.5194/GMD-8-1339-2015>

1263 Müller, D., Ansmann, A., Mattis, I., Tesche, M., Wandinger, U., Althausen, D., & Pisani, G. (2007).
1264 Aerosol-type-dependent lidar ratios observed with Raman lidar. *Journal of Geophysical Research
1265 Atmospheres*, 112(16). <https://doi.org/10.1029/2006JD008292>

1266 Müller, D., Böckmann, C., Kolgotin, A., Schneidenbach, L., Chemyakin, E., Rosemann, J., Znak, P., &
1267 Romanov, A. (2016). Microphysical particle properties derived from inversion algorithms developed
1268 in the framework of EARLINET. *Atmospheric Measurement Techniques*, 9(10), 5007–5035.
1269 <https://doi.org/10.5194/AMT-9-5007-2016>

1270 Müller, D., Mattis, I., Wandinger, U., Ansmann, A., Althausen, D., & Stohl, A. (2005). Raman lidar
1271 observations of aged Siberian and Canadian forest fire smoke in the free troposphere over Germany
1272 in 2003: Microphysical particle characterization. In *Journal of Geophysical Research D: Atmospheres*
1273 (Vol. 110, Issue 17). <https://doi.org/10.1029/2004JD005756>

1274 Müller, D., Wandinger, U., & Ansmann, A. (1999). Microphysical particle parameters from extinction and
1275 backscatter lidar data by inversion with regularization: theory. *Applied Optics*, 38(12), 2346.
1276 <https://doi.org/10.1364/AO.38.002346>

1277 Nam, C., Bony, S., Dufresne, J. L., & Chepfer, H. (2012). The too few, too bright tropical low-cloud
1278 problem in CMIP5 models. *Geophysical Research Letters*, 39(21).
1279 <https://doi.org/10.1029/2012GL053421>

1280 [Omar, A. H., Winker, D. M., Kittaka, C., Vaughan, M. A., Liu, Z., Hu, Y., Trepte, C. R., Rogers, R. R.,](#)
1281 [Ferrare, R. A., Lee, K. P., Kuehn, R. E., & Hostetler, C. A. \(2009\). The CALIPSO automated aerosol](#)
1282 [classification and lidar ratio selection algorithm. *Journal of Atmospheric and Oceanic Technology*,](#)
1283 [26\(10\), 1994–2014. <https://doi.org/10.1175/2009JTECHA1231.1>](#)

1284 [Paasonen, P., Asmi, A., Petäjä, T., Kajos, M. K., Äijälä, M., Junninen, H., Holst, T., Abbatt, J. P. D., Arneth,](#)
1285 [A., Birmili, W., van der Gon, H. D., Hamed, A., Hoffer, A., Laakso, L., Laaksonen, A., Richard](#)
1286 [Leaich, W., Plass-Dülmer, C., Pryor, S. C., Räisänen, P., ... Kulmala, M. \(2013\). Warming-induced](#)
1287 [increase in aerosol number concentration likely to moderate climate change. *Nature Geoscience*, 6\(6\),](#)
1288 [438–442. <https://doi.org/10.1038/NGEO1800>](#)

1289 [Patel, P. N., Gautam, R., Michibata, T., & Gadhavi, H. \(2019\). Strengthened Indian Summer Monsoon](#)
1290 [Precipitation Susceptibility Linked to Dust-Induced Ice Cloud Modification. *Geophysical Research*](#)
1291 [Letters, 46\(14\), 8431–8441. <https://doi.org/10.1029/2018GL081634>](#)

1292 [Patel, P. N., & Jiang, J. H. \(2021\). Cloud condensation nuclei characteristics at the Southern Great Plains](#)
1293 [site: role of particle size distribution and aerosol hygroscopicity. *Environmental Research*](#)
1294 [Communications, 3\(7\), 075002. <https://doi.org/10.1088/2515-7620/AC0E0B>](#)

1295 [Patel, P. N., & Kumar, R. \(2016\). Dust Induced Changes in Ice Cloud and Cloud Radiative Forcing over a](#)
1296 [High Altitude Site. *Aerosol and Air Quality Research*, 16\(8\), 1820–1831.](#)
1297 [<https://doi.org/10.4209/aaqr.2015.05.0325>](#)

1298 [Patel, P. N., Quaas, J., & Kumar, R. \(2017\). A new statistical approach to improve the satellite-based](#)
1299 [estimation of the radiative forcing by aerosol–cloud interactions. *Atmospheric Chemistry and Physics*,](#)
1300 [17\(5\), 3687–3698. <https://doi.org/10.5194/acp-17-3687-2017>](#)

1301 [Pérez-Ramírez, D., Whiteman, D. N., Veselovskii, I., Kolgotin, A., Korenskiy, M., & Alados-Arboledas,](#)
1302 [L. \(2013\). Effects of systematic and random errors on the retrieval of particle microphysical properties](#)
1303 [from multiwavelength lidar measurements using inversion with regularization. *Atmospheric*](#)
1304 [Measurement Techniques, 6\(11\), 3039–3054. <https://doi.org/10.5194/AMT-6-3039-2013>](#)

1305 [Petters, M. D., Carrico, C. M., Kreidenweis, S. M., Prenni, A. J., DeMott, P. J., Collett, J. L., & Moosmüller,](#)
1306 [H. \(2009\). Cloud condensation nucleation activity of biomass burning aerosol. *Journal of Geophysical*](#)
1307 [Research Atmospheres, 114\(22\), 1–16. <https://doi.org/10.1029/2009JD012353>](#)

1308 [Petters, M. D., & Kreidenweis, S. M. \(2007\). A single parameter representation of hygroscopic growth and](#)
1309 [cloud condensation nucleus activity. *Atmospheric Chemistry and Physics*, 7\(8\), 1961–1971.](#)
1310 [<https://doi.org/10.5194/ACP-7-1961-2007>](#)

1311 [Quaas, J., Boucher, O., Bellouin, N., & Kinne, S. \(2008\). Satellite-based estimate of the direct and indirect](#)
1312 [aerosol climate forcing. *Journal of Geophysical Research Atmospheres*, 113\(5\),](#)
1313 [<https://doi.org/10.1029/2007JD008962>](#)

1314 [Quaas, J., Ming, Y., Menon, S., Takemura, T., Wang, M., Penner, J. E., Gettelman, A., Lohmann, U.,](#)
1315 [Bellouin, N., Boucher, O., Sayer, A. M., Thomas, G. E., McComiskey, A., Feingold, G., Hoose, C.,](#)
1316 [Kristjánsson, J. E., Liu, X., Balkanski, Y., Donner, L. J., ... Schulz, M. \(2009\). Aerosol indirect effects](#)
1317 [- general circulation model intercomparison and evaluation with satellite data. *Atmospheric Chemistry*](#)
1318 [and Physics, 9\(22\), 8697–8717. <https://doi.org/10.5194/acp-9-8697-2009>](#)

1319 [Redemann, J., Wood, R., Zuidema, P., Doherty, S. J., Luna, B., LeBlanc, S. E., Diamond, M. S., Shinozuka,](#)
1320 [Y., Chang, I. Y., Ueyama, R., Pfister, L., Ryoo, J. M., Dobracki, A. N., da Silva, A. M., Longo, K.](#)

1321 [M., Kacenelenbogen, M. S., Flynn, C. J., Pistone, K., Knox, N. M., ... Gao, L. \(2021\). An overview](#)
1322 [of the ORACLES \(ObseRvations of Aerosols above CLouds and their intEractionS\) project: aerosol-](#)
1323 [cloud-radiation interactions in the Southeast Atlantic basin. *Atmos. Chem. Phys.*, 21\(3\), 1507–1563.](#)
1324 <https://doi.org/10.5194/acp-21-1507-2021>

1325 [Roberts, G. C., & Nenes, A. \(2005\). A continuous-flow streamwise thermal-gradient CCN chamber for](#)
1326 [atmospheric measurements. *Aerosol Science and Technology*, 39\(3\), 206–221.](#)
1327 <https://doi.org/10.1080/027868290913988>

1328 [Rose, D., Gunthe, S. S., Mikhailov, E., Frank, G. P., Dusek, U., Andreae, M. O., & Pöschl, U. \(2008\).](#)
1329 [Calibration and measurement uncertainties of a continuous-flow cloud condensation nuclei counter](#)
1330 [\(DMT-CCNC\): CCN activation of ammonium sulfate and sodium chloride aerosol particles in theory](#)
1331 [and experiment. *Atmospheric Chemistry and Physics*, 8\(5\), 1153–1179. https://doi.org/10.5194/ACP-](#)
1332 [8-1153-2008](#)

1333 [Rosenfeld, D. \(2008\). Flood or drought: how do aerosols affect precipitation? *Science*, 321, 1309–1313.](#)

1334 [Rosenfeld, D., Andreae, M. O., Asmi, A., Chin, M., Leeuw, G., Donovan, D. P., Kahn, R., Kinne, S.,](#)
1335 [Kivekäs, N., Kulmala, M., Lau, W., Schmidt, K. S., Suni, T., Wagner, T., Wild, M., & Quaas, J.](#)
1336 [\(2014\). Global observations of aerosol-cloud-precipitation- climate interactions. *Rev. Geophys.*, 52,](#)
1337 [750–808. https://doi.org/10.1002/2013RG000441](#)

1338 [Rosenfeld, D., Zheng, Y., Hashimshoni, E., Pöhlker, M. L., Jefferson, A., Pöhlker, C., Yu, X., Zhu, Y., Liu,](#)
1339 [G., Yue, Z., Fischman, B., Li, Z., Giguzin, D., Goren, T., Artaxo, P., Barbosa, H. M. J., Pöschl, U., &](#)
1340 [Andreae, M. O. \(2016\). Satellite retrieval of cloud condensation nuclei concentrations by using clouds](#)
1341 [as CCN chambers. *Proceedings of the National Academy of Sciences*.](#)
1342 <https://doi.org/10.1073/pnas.1514044113>

1343 [Saito, M., Yang, P., Ding, J., & Liu, X. \(2021\). A Comprehensive Database of the Optical Properties of](#)
1344 [Irregular Aerosol Particles for Radiative Transfer Simulations. *Journal of the Atmospheric Sciences*,](#)
1345 [78\(7\), 2089–2111. https://doi.org/10.1175/JAS-D-20-0338.1](#)

1346 [Seinfeld, J. H., Bretherton, C., Carslaw, K. S., Coe, H., DeMott, P. J., Dunlea, E. J., Feingold, G., Ghan, S.,](#)
1347 [Guenther, A. B., Kahn, R., Kraucunas, I., Kreidenweis, S. M., Molina, M. J., Nenes, A., Penner, J. E.,](#)
1348 [Prather, K. A., Ramanathan, V., Ramaswamy, V., Rasch, P. J., ... Wood, R. \(2016\). Improving our](#)
1349 [fundamental understanding of the role of aerosol–cloud interactions in the climate system.](#)
1350 [*Proceedings of the National Academy of Sciences*, 113\(21\), 5781–5790.](#)
1351 <https://doi.org/10.1073/pnas.1514043113>

1352 [Shinozuka, Y., Clarke, A. D., Nenes, A., Jefferson, A., Wood, R., McNaughton, C. S., Ström, J., Tunved,](#)
1353 [P., Redemann, J., Thornhill, K. L., Moore, R. H., Latham, T. L., Lin, J. J., & Yoon, Y. J. \(2015\). The](#)
1354 [relationship between cloud condensation nuclei \(CCN\) concentration and light extinction of dried](#)
1355 [particles: Indications of underlying aerosol processes and implications for satellite-based CCN](#)
1356 [estimates. *Atmospheric Chemistry and Physics*, 15\(13\), 7585–7604. https://doi.org/10.5194/ACP-15-](#)
1357 [7585-2015](#)

1358 [Shipley, S. T., Tracy, D. H., Eloranta, E. W., Trauger, J. T., Sroga, J. T., Roesler, F. L., & Weinman, J. A.](#)
1359 [\(1983\). HIGH SPECTRAL RESOLUTION LIDAR TO MEASURE OPTICAL SCATTERING](#)
1360 [PROPERTIES OF ATMOSPHERIC AEROSOLS. 1: THEORY AND INSTRUMENTATION.](#)
1361 [*Applied Optics*, 22\(23\), 3716–3724. https://doi.org/10.1364/AO.22.003716](#)

1362 Stier, P. (2016). Limitations of passive remote sensing to constrain global cloud condensation nuclei.
1363 *Atmospheric Chemistry and Physics*, 16(10), 6595–6607. <https://doi.org/10.5194/ACP-16-6595-2016>

1364 Tan, W., Zhao, G., Yu, Y., Li, C., Li, J., Kang, L., Zhu, T., & Zhao, C. (2019). Method to retrieve cloud
1365 condensation nuclei number concentrations using lidar measurements. *Atmospheric Measurement*
1366 *Techniques*, 12(7), 3825–3839. <https://doi.org/10.5194/AMT-12-3825-2019>

1367 Tesche, M., Ansmann, A., Müller, D., Althausen, D., Engelmann, R., Freudenthaler, V., & Groß, S. (2009).
1368 Vertically resolved separation of dust and smoke over Cape Verde using multiwavelength Raman and
1369 polarization lidars during Saharan Mineral Dust Experiment 2008. *Journal of Geophysical Research*
1370 *Atmospheres*, 114(13). <https://doi.org/10.1029/2009JD011862>

1371 Titos, G., Cazorla, A., Zieger, P., Andrews, E., Lyamani, H., Granados-Muñoz, M. J., Olmo, F. J., &
1372 Alados-Arboledas, L. (2016). Effect of hygroscopic growth on the aerosol light-scattering coefficient:
1373 A review of measurements, techniques and error sources. *Atmospheric Environment*, 141, 494–507.
1374 <https://doi.org/10.1016/J.ATMOSENV.2016.07.021>

1375 Torres, B., Dubovik, O., Fuertes, D., Schuster, G., Eugenia Cachorro, V., Lapyonok, T., Goloub, P., Blarel,
1376 L., Barreto, A., Mallet, M., Toledano, C., & Tanré, D. (2017). Advanced characterisation of aerosol
1377 size properties from measurements of spectral optical depth using the GRASP algorithm. *Atmospheric*
1378 *Measurement Techniques*, 10(10), 3743–3781. <https://doi.org/10.5194/AMT-10-3743-2017>

1379 Vaughan, M., Pitts, M., Trepte, C., Winker, D., Detweiler, P., Garnier, A., Getzewich, B., Hunt, W.,
1380 Lamberth, J., Lee, K.-P., Lucker, P., Murray, T., Rodier, S., Tremas, T., Bazureau, A., & Pelon, J.
1381 (2017). *Cloud - Aerosol LIDAR Infrared Pathfinder Satellite Observations (CALIPSO), Data*
1382 *Management System, Data Products Catalog, Document No: PC-SCI-503, Release 4.10.*
1383 https://doi.org/https://www-calipso.larc.nasa.gov/products/CALIPSO_DPC_Rev4x10.pdf

1384 Veselovskii, I., Dubovik, O., Kolgotin, A., Korenskiy, M., Whiteman, D. N., Allakhverdiev, K., &
1385 Huseyinoglu, F. (2012). Linear estimation of particle bulk parameters from multi-wavelength lidar
1386 measurements. *Atmospheric Measurement Techniques*, 5(5), 1135–1145.
1387 <https://doi.org/10.5194/AMT-5-1135-2012>

1388 Veselovskii, I., Kolgotin, A., Griaznov, V., Müller, D., Franke, K., & Whiteman, D. N. (2004). Inversion
1389 of multiwavelength Raman lidar data for retrieval of bimodal aerosol size distribution. *Applied Optics*,
1390 43(5), 1180–1195. <https://doi.org/10.1364/AO.43.001180>

1391 Veselovskii, I., Kolgotin, A., Griaznov, V., Müller, D., Wandinger, U., & Whiteman, D. N. (2002).
1392 Inversion with regularization for the retrieval of tropospheric aerosol parameters from
1393 multiwavelength lidar sounding. *Applied Optics*, 41(18), 3685. <https://doi.org/10.1364/AO.41.003685>

1394 Wang, Y., Li, Z., Zhang, Y., Du, W., Zhang, F., Tan, H., Xu, H., Fan, T., Jin, X., Fan, X., Dong, Z., Wang,
1395 Q., & Sun, Y. (2018). Characterization of aerosol hygroscopicity, mixing state, and CCN activity at a
1396 suburban site in the central North China Plain. *Atmospheric Chemistry and Physics*, 18(16), 11739–
1397 11752. <https://doi.org/10.5194/acp-18-11739-2018>

1398 Winker, D. M., Hunt, W. H., & McGill, M. J. (2007). Initial performance assessment of CALIOP.
1399 *Geophysical Research Letters*, 34(19). <https://doi.org/10.1029/2007GL030135>

1400 Xu, F., Gao, L., Redemann, J., Flynn, C. J., Espinosa, W. R., da Silva, A. M., Stamnes, S., Burton, S. P.,
1401 Liu, X., Ferrare, R., Cairns, B., & Dubovik, O. (2021). A Combined Lidar-Polarimeter Inversion

1402 [Approach for Aerosol Remote Sensing Over Ocean. *Frontiers in Remote Sensing*, 0, 2.](https://doi.org/10.3389/FRSEN.2021.620871)
 1403 <https://doi.org/10.3389/FRSEN.2021.620871>

1404 [Yang, P., Feng, Q., Hong, G., Kattawar, G. W., Wiscombe, W. J., Mishchenko, M. I., Dubovik, O., Laszlo,
 1405 L., & Sokolik, I. N. \(2007\). Modeling of the scattering and radiative properties of nonspherical dust-
 1406 like aerosols. *Journal of Aerosol Science*, 38\(10\), 995–1014.
 1407 <https://doi.org/10.1016/J.JAEROSCI.2007.07.001>](https://doi.org/10.1016/J.JAEROSCI.2007.07.001)

1408 [Young, S. A., & Vaughan, M. A. \(2009\). The retrieval of profiles of particulate extinction from cloud-
 1409 aerosol lidar infrared pathfinder satellite observations \(CALIPSO\) data: Algorithm description.
 1410 *Journal of Atmospheric and Oceanic Technology*, 26\(6\), 1105–1119.
 1411 <https://doi.org/10.1175/2008JTECHA1221.1>](https://doi.org/10.1175/2008JTECHA1221.1)

1412 [Yu, H., Chin, M., Winker, D. M., Omar, A. H., Liu, Z., Kittaka, C., & Diehl, T. \(2010\). Global view of
 1413 aerosol vertical distributions from CALIPSO lidar measurements and GOCART simulations:
 1414 Regional and seasonal variations. *Journal of Geophysical Research Atmospheres*, 115\(4\), 1–19.
 1415 <https://doi.org/10.1029/2009JD013364>](https://doi.org/10.1029/2009JD013364)

1416 ✖

Deleted: Andreae, M. O., & Rosenfeld, D. (2008). Aerosol-cloud-precipitation interactions. Part 1. The nature and sources of cloud-active aerosols. *Earth-Science Reviews*, 89(1–2), 13–41. <https://doi.org/10.1016/j.earscirev.2008.03.001>

Bedoya-Velásquez, A. E., Navas-Guzmán, F., Granados-Muñoz, M. J., Titos, G., Román, R., Andrés Casquero-Vera, J., Ortiz-Amezcu, P., Antonio Benavent-Oltra, J., de Arruda Moreira, G., Montilla-Rosero, E., Hoyos, C. D., Artiñano, B., Coz, E., Olmo-Reyes, F. J., Alados-Arboledas, L., & Guerrero-Rascado, J. L. (2018). Hygroscopic growth study in the framework of EARLINET during the SLOPE i campaign: Synergy of remote sensing and in situ instrumentation. *Atmospheric Chemistry and Physics*, 18(10), 7001–7017. <https://doi.org/10.5194/ACP-18-7001-2018>

Bi, L., Yang, P., Kattawar, G. W., & Kahn, R. (2009). Single-scattering properties of triaxial ellipsoidal particles for a size parameter range from the Rayleigh to geometric-optics regimes. *Applied Optics*, 48(1), 114–126. <https://doi.org/10.1364/AO.48.000114>

Bohren, C. F., & Huffman, D. R. (1998). Absorption and Scattering of Light by Small Particles. *Absorption and Scattering of Light by Small Particles*. <https://doi.org/10.1002/9783527618156>

Braun, S., Stephens, G., Berndt, E., Blanchard, Y., Blanchet, J.-P., Carmichael, G., da Silva, A., Ferrare, R., Ivancu, M., Kacenenbogen, M., Kirschbaum, D., Libois, Q., Mace, G., Omar, A., Petersen, W., Redemann, J., Seidel, F., van den Heever, S., Waliser, D., & Winker, D. (2022). *Aerosol, Cloud, Convection, and Precipitation (ACCP) Science & Applications*. [https://aos.gsfc.nasa.gov/docs/ACCP_Science_Narrative-\(Mar2022\).pdf](https://aos.gsfc.nasa.gov/docs/ACCP_Science_Narrative-(Mar2022).pdf)

Brock, C. A., Wagner, N. L., Anderson, B. E., Attwood, A. R., Beyersdorf, A., Campuzano-Jost, P., Carlton, A. G., Day, D. A., Diskin, G. S., Gordon, T. D., Jimenez, J. L., Lack, D. A., Liao, J., Markovic, M. Z., Middlebrook, A. M., Ng, N. L., Perring, A. E., Richardson, M. S., Schwarz, J. P., ... Murphy, D. M. (2016). Aerosol optical properties in the southeastern United States in summer - Part 1: Hygroscopic growth. *Atmospheric Chemistry and Physics*, 16(8), 4987–5007. <https://doi.org/10.5194/ACP-16-4987-2016>

Burkart, J., Steiner, G., Reischl, G., & Hitzenberger, R. (2011). Long-term study of cloud condensation nuclei (CCN) activation of the atmospheric aerosol in Vienna. *Atmospheric Environment*, 45(32), 5751–5759. <https://doi.org/10.1016/J.ATMOSENV.2011.07.022>

Burton, S. P., Chemyakin, E., Liu, X., Knobelspiess, K., Starnes, S., Sawamura, P., Moore, R. H., Hostetler, C. A., & Ferrare, R. A. (2016). Information content and sensitivity of the $3\beta + 2\alpha$ lidar measurement system for aerosol microphysical retrievals. *Atmospheric Measurement Techniques*, 9(11), 5555–5574. <https://doi.org/10.5194/AMT-9-5555-2016>

Burton, S. P., Ferrare, R. A., Hostetler, C. A., Hair, J. W., Rogers, R. R., Obland, M. D., Butler, C. F., Cook, A. L., Harper, D. B., & Froyd, K. D. (2012). Aerosol classification using airborne High Spectral Resolution Lidar measurements-methodology and examples. (... [2])

1555
1556
1557
1558

Table 1: Typical parameter ranges for the aerosol bimodal distribution used in our study to construct the LUTs. V_f^t / V_c^t is the ratio of the volume concentration of the fine mode to the coarse mode. m_R and m_I represent the mean values of real and imaginary parts of the complex refractive index.

Deleted: ¶
Formatted: Font: Bold
Formatted: Font: Not Bold

Aerosol Parameters	Marine	Dust	Polluted Continental	Clean Continental	Biomass burning
r_f^v	0.065-0.085	0.062-0.082	0.075-0.095	0.08-0.11	0.072-0.082
r_c^v	0.5-0.6	0.59-0.64	0.6-0.71	0.42-0.52	0.75-0.80
σ_f^v	0.46-0.54	0.4-0.53	0.38-0.46	0.37-0.45	0.4-0.47
σ_c^v	0.68-0.78	0.6-0.7	0.65-0.75	0.70-0.80	0.65-0.75
V_f^t / V_c^t	0.1-0.25	0.1-0.5	1.0-2.0	0.01-0.15	1.5-2.5
m_R / m_I	1.36/0.0015	1.56/0.001	1.47/0.014	1.401/0.003	1.51/0.021
κ	0.7	0.03	0.27	0.31	0.1

Formatted Table

1559
1560
1561

Table 2: CCN errors at six supersaturation (SS) retrieved from error-free inputs for the five aerosol types.

Deleted: /
Deleted: .

Aerosol Types	CCN error (%)					
	0.07%	0.1%	0.2%	0.4%	0.8%	1.0%
Marine	-0.00 ± 0.21	-0.01 ± 0.23	0.00 ± 0.26	-0.00 ± 0.25	0.00 ± 0.23	-0.00 ± 0.24
Dust	-0.01 ± 0.22	-0.01 ± 0.23	0.00 ± 0.26	-0.01 ± 0.24	0.00 ± 0.25	-0.01 ± 0.23
Mean ± SD (%) Polluted continental	-0.01 ± 0.18	0.00 ± 0.18	-0.01 ± 0.16	0.00 ± 0.18	-0.01 ± 0.19	-0.00 ± 0.18
Clean continental	-0.01 ± 0.19	-0.01 ± 0.20	-0.01 ± 0.19	-0.00 ± 0.17	-0.00 ± 0.18	-0.01 ± 0.17
Smoke	-0.01 ± 0.19	-0.01 ± 0.21	-0.01 ± 0.18	-0.01 ± 0.20	-0.00 ± 0.22	-0.01 ± 0.19

1562

1567

1568

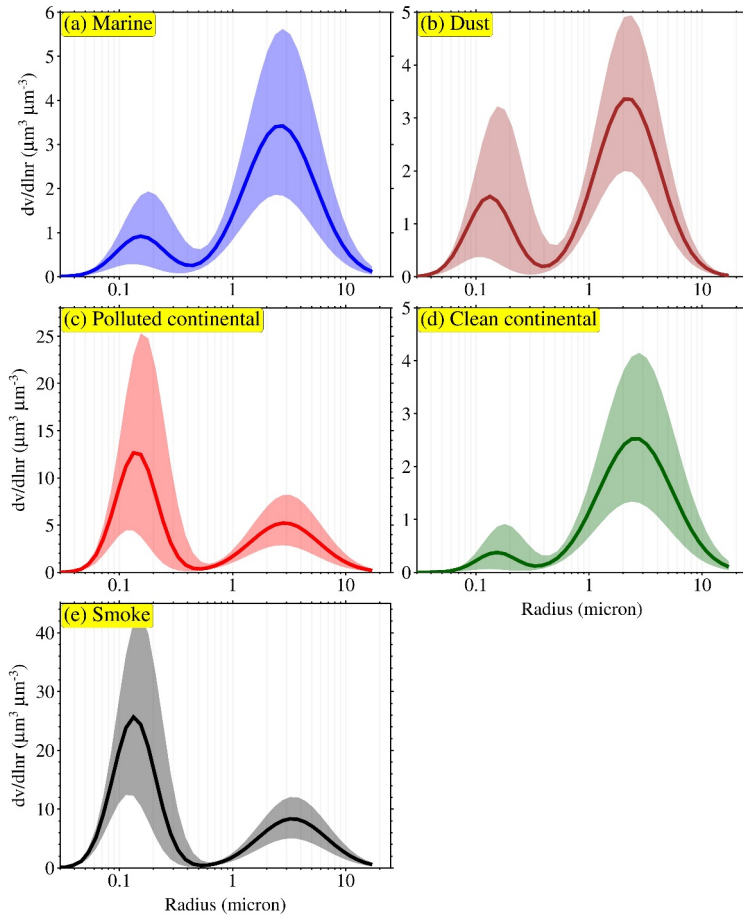
1569 **Table 3:** Sensitivity of CCN retrieval to the bimodal fits at different supersaturation ratios from
1570 the 100 aerosol size distributions obtained from ARM-SGP. The CCN error is calculated as an
1571 absolute value.

Deleted: 2

	CCN error (%)					
	0.07%	0.1%	0.2%	0.4%	0.8%	1.0%
Mean ± SD (%)	3.3 ± 2.4	3.9 ± 2.8	3.1 ± 2.7	2.9 ± 1.8	2.1 ± 1.5	1.7 ± 1.3

1572

1573



1576

1577

1578

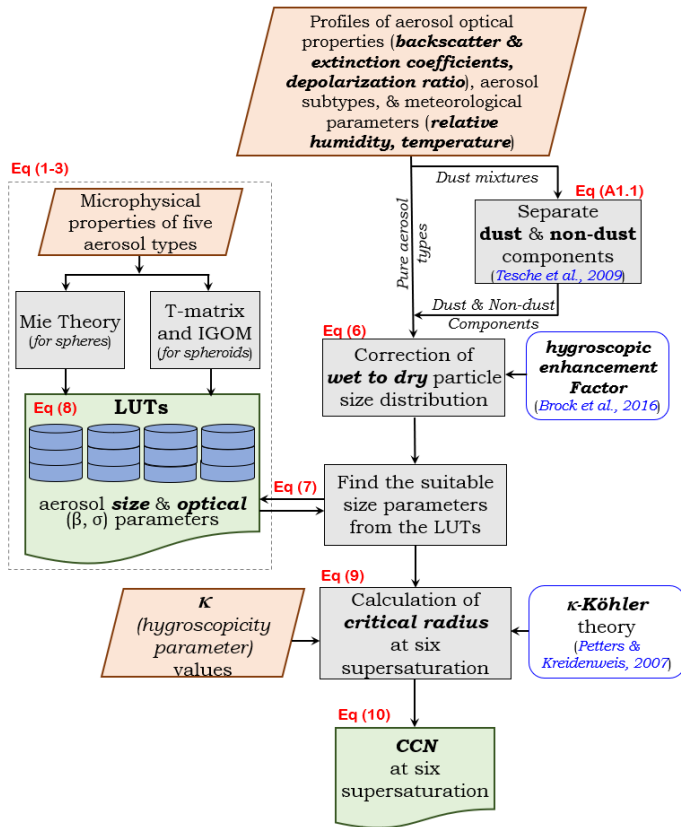
1579

1580

1581

1582

Figure 1: Bimodal log-normal particle size distributions for five aerosol types (marine, dust, polluted continental, clean continental and smoke aerosols) considered in this study to build the look-up-tables (LUTs). These particle size distributions were derived using measurements from sun/sky radiometer at multiple selected Aerosol Robotic Network (AERONET) sites. Solid line represents the mean of particle size distribution, whereas the shaded area shows the range of size distribution covers in the respective LUTs.



1584

1585

1586

1587

1588

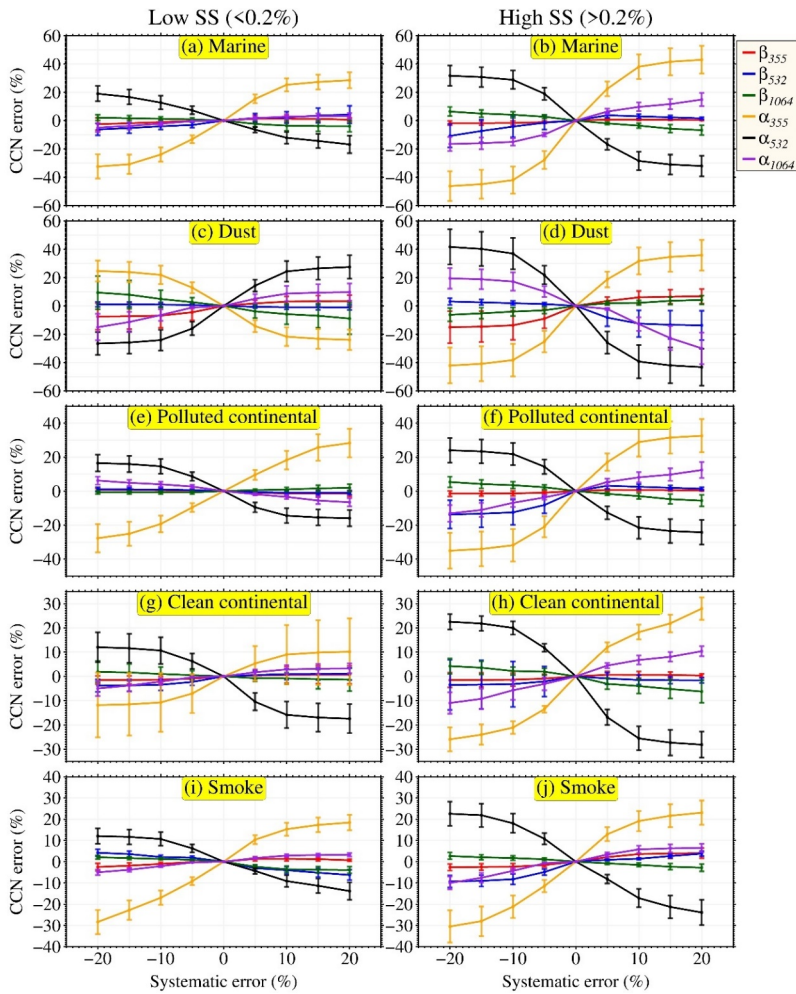
1589

1590

1591

Figure 2: Flowchart of ECLiAP algorithm for the retrieval of N_{CCN} from lidar measurements. The steps within the dotted line box describes the pre-processing which includes the calculation of aerosol optical properties using Mie scattering theory (T-matrix/IGOM for dust) to build look-up-tables for five aerosol models. The steps outside the dotted line box represent the retrieval process of N_{CCN} from the given inputs of aerosol optical properties and meteorological parameters. The chart also refers to the used equations associated to the particular retrieval process.

Deleted: →



1594

1595

1596

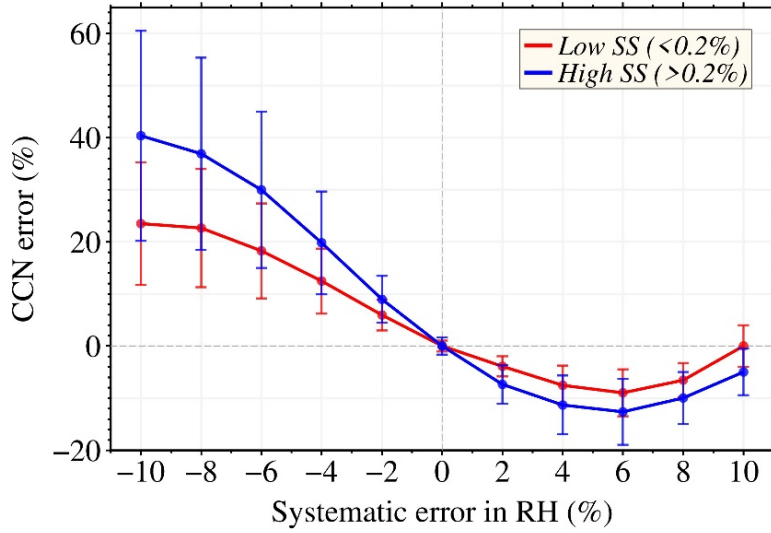
1597

1598

Figure 3: Systematic errors in retrieved N_{CCN} . This represent the errors in retrieved N_{CCN} as a function of systematic errors in backscatter and extinction coefficients at all three wavelengths for low ($\leq 0.2\%$) and high ($> 0.2\%$) supersaturations and for all five aerosol subtypes as. The markers denote the mean value and the error bars represent the standard deviation.

1599

1600



1601

1602

1603

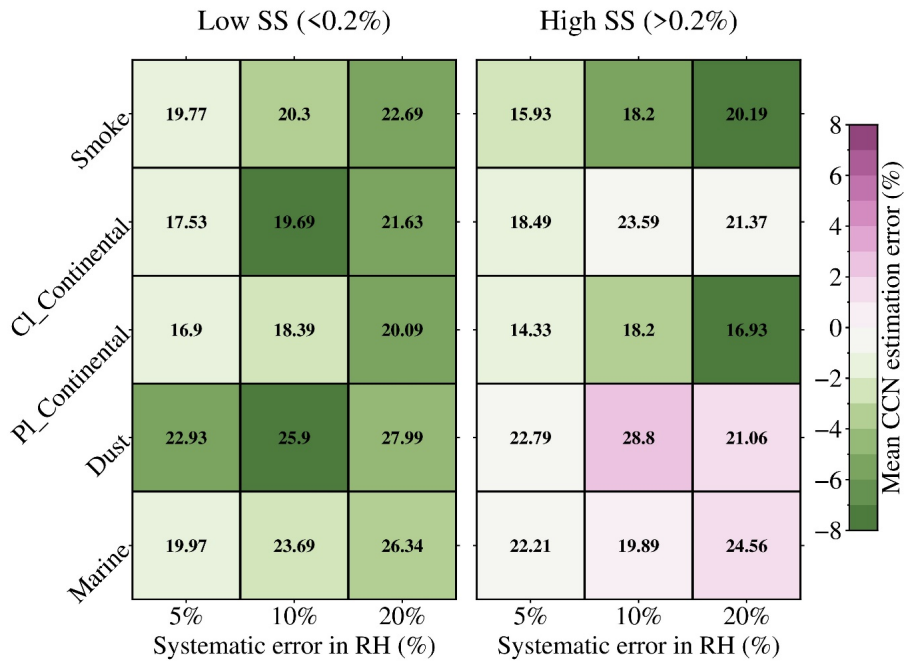
1604

1605

Figure 4: Systematic errors in retrieved N_{CCN} . This represent the errors in retrieved N_{CCN} as a function of systematic error in RH, combines for all aerosol subtypes, at low ($\leq 0.2\%$) and high ($> 0.2\%$) supersaturations. The markers denote the mean value and the error bars represent the standard deviation.

1606

1607



1608

1609

1610

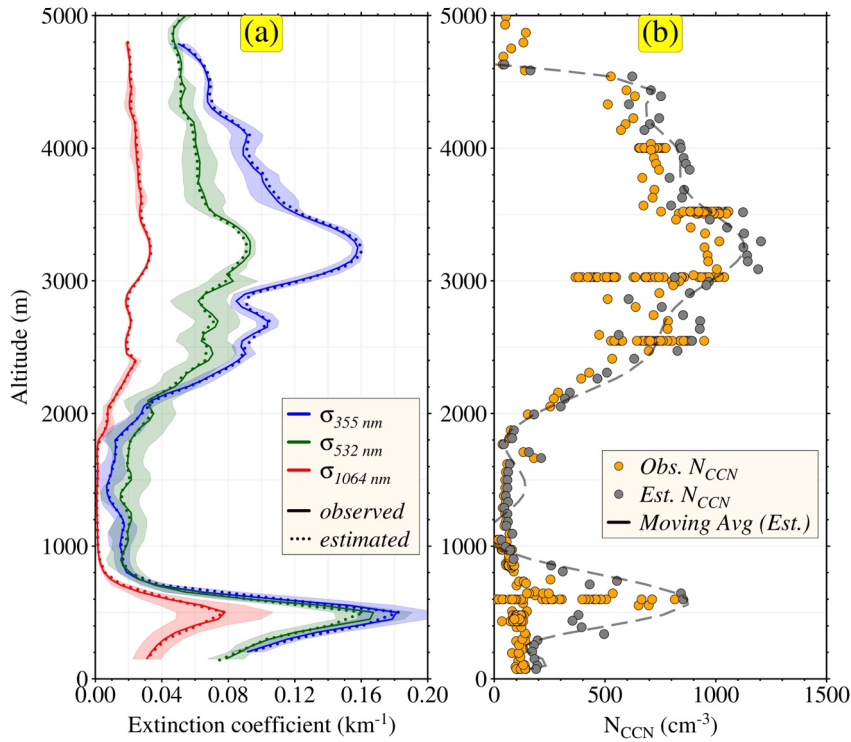
1611

1612

1613

Figure 5: Random errors in retrieved N_{CCN} . This represents the random errors in retrieved N_{CCN} at low ($\leq 0.2\%$) and high ($> 0.2\%$) supersaturations with different random error conditions individually for five aerosol subtypes. The uncertainty of backscatter and extinction coefficients off all the tests is 10% and the uncertainties of RH are 5%, 10% and 20%. The color shows the mean values whereas number shows the ± 1 standard deviation of errors.

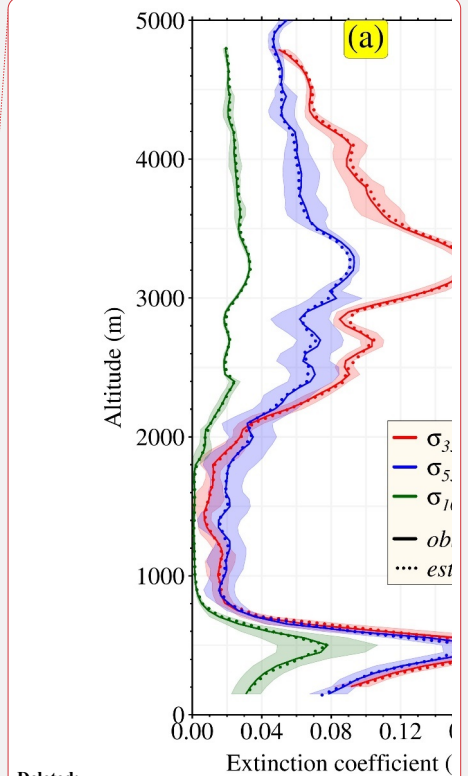
Deleted: represent



1616

1617 **Figure 6: Comparison between retrieved and observed vertical profiles of aerosol extinction**
 1618 **coefficients and N_{CCN} .** The ECLiAP retrieved (a) aerosol extinction coefficients at 355, 532 and
 1619 1064 nm and (b) N_{CCN} were compared against the one observed during NASA ORACLE'S
 1620 airborne campaign. The lidar signals were mainly influenced by the mixture of smoke and
 1621 dust or marine aerosols. The relationship between HSRL-2 measured aerosol extinction
 1622 coefficients (solid lines) and retrieved (dotted line) by an algorithm in the left panel. The right
 1623 panel illustrates the comparison of retrieved N_{CCN} using lidar measurements and measured by
 1624 CCN counter. The dashed line in the right panel shows the moving average of retrieved N_{CCN}
 1625 values. CCN counter measured N_{CCN} at supersaturation ranging from 0.32%-0.34% for the
 1626 selected region (described in Figure S4), therefore, the retrieval of N_{CCN} was carried out at
 1627 supersaturation of 0.34%.

Deleted: ¶



Deleted:

Formatted: Caption

Deleted: .

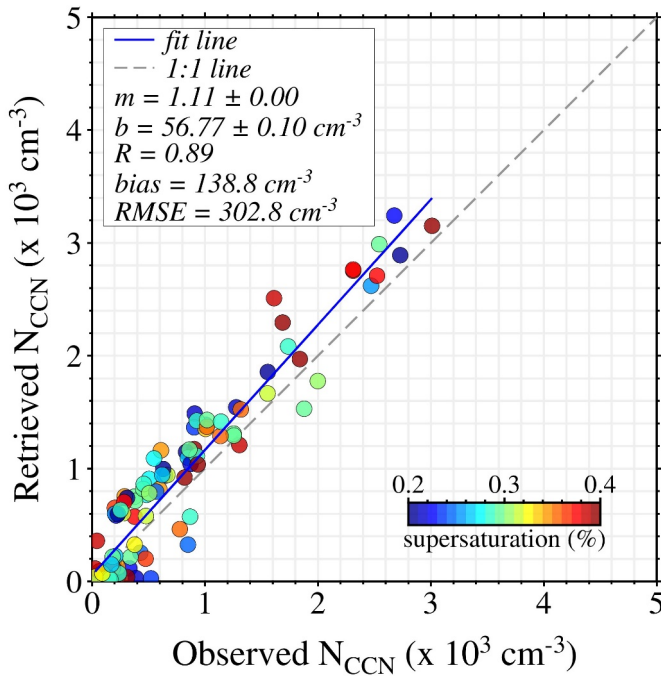
Deleted: Right

Deleted: and

Deleted: ¶

1634

1635

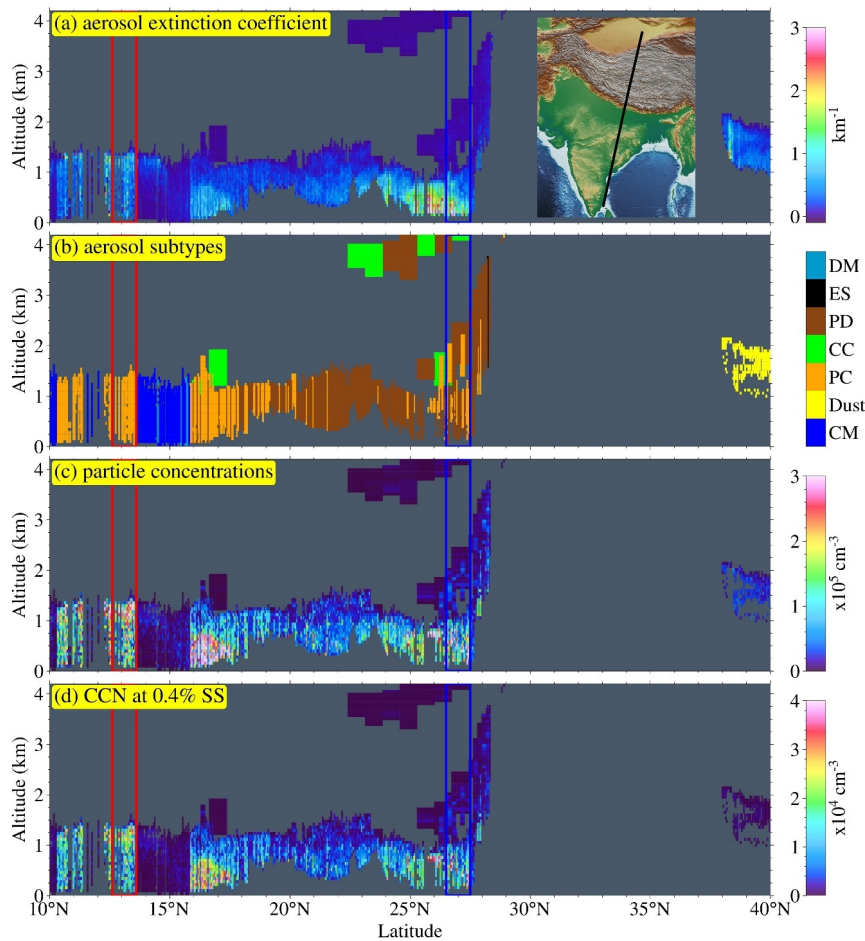


1636

1637 **Figure 7: Comparison between retrieved and observed N_{CCN} .** The comparison between ECLiAP
1638 retrieved N_{CCN} from HSRL-2 lidar measurements and the measured N_{CCN} values from CCN
1639 counter. The HSRL-2 and CCN counter data were collected from the multiple flights during NASA-
1640 ORACLES airborne campaigns conducted in 2017-2018. The color bar displays the observed
1641 values of supersaturation for each measurement and the N_{CCN} were retrieved on the same
1642 supersaturation for the direct comparison. The slope and intercept of the best fit line are given in
1643 the key by m and b , respectively. The gray dash line indicates the unit slope line and blue solid
1644 line indicates the regression line.

Deleted: ORCLES

1645



1648

1649

1650

1651

1652

1653

1654

1655

Figure 8: Retrieval from spaceborne lidar measurements. Explore the capability of ECLiAP, the N_{CN} and N_{CCN} retrieved from CALIOP onboard CALIPSO observations on 01 January 2019, passing over the Tibetan plateau and Indian landmass. CALIOP derived (a) extinction coefficient at 532 nm, (b) aerosol subtypes were shown in the upper two panels. The lower two panels illustrate the ECLiAP retrieved (c) total particle concentrations (N_{CN}), and (d) N_{CCN} at supersaturation 0.4%. The two color boxes in red (case-I) and blue (case-II) are the two different scenarios that are further studied to assess the capability of ECLiAP.

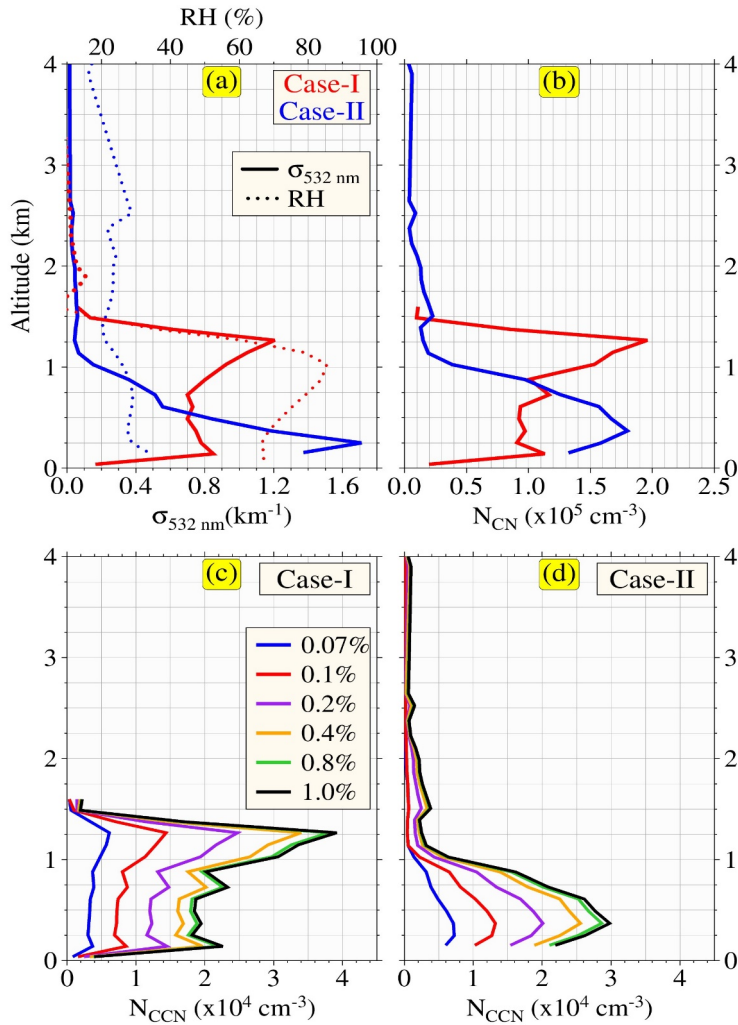
Deleted: during

Deleted: Lower

Deleted: panel

Deleted: scenario

Deleted: which



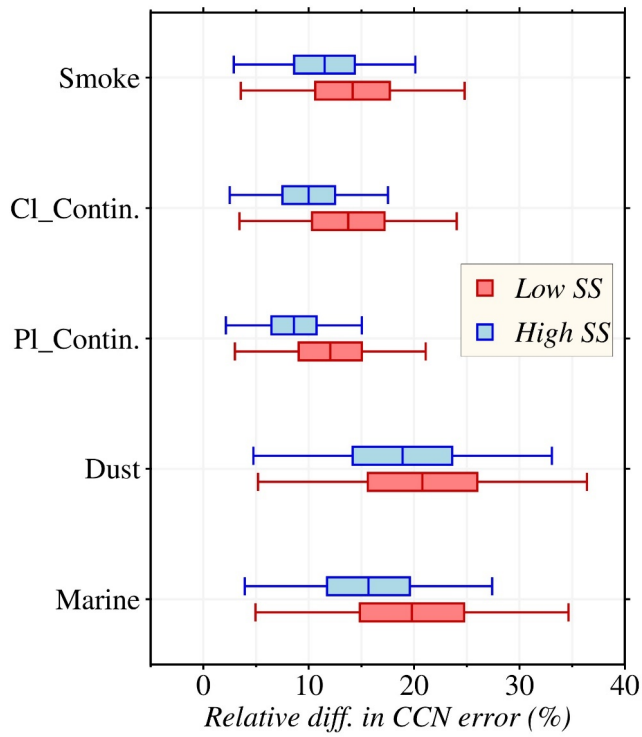
1662
 1663
 1664
 1665
 1666
 1667

Figure 9: Case studied from CALIOP observations. As per mentioned above, two different scenarios (*case-I dominated by polluted continental and case-II contains a mixture of polluted continental and polluted dust*) were identified and studied in detail to assess the potential of ECLiAP to accurately capture the particles physicochemical characteristics and their influence on the retrieved values along with meteorological influence.

- Deleted: studies
- Deleted: details
- Deleted: O
- Deleted: capturing

1672

1673



1674

1675 **Figure 10: Relative difference in CCN error between $3\beta+2\alpha$ and $3\beta+3\alpha$.** The CCN error were
1676 calculated against the given inputs using Eq. (11) for both the $3\beta+2\alpha$ and $3\beta+3\alpha$ techniques
1677 individually. Later the relative difference of CCN error has calculated from the individual CCN
1678 errors at low and high supersaturations for each aerosol subtypes.

Formatted: Centered

Page 23: [1] Deleted Piyushkumar Patel 7/29/23 1:01:00 PM



Page 33: [2] Deleted Piyushkumar Patel 7/29/23 3:59:00 PM

